

Modelling the vibration of tyre sidewalls

W R Graham

University of Cambridge, Department of Engineering, Trumpington Street, Cambridge, CB2 1PZ

Abstract

The dynamical behaviour of the sidewall has an important influence on tyre vibration characteristics. Nonetheless, it remains crudely represented in many existing models. The current work considers a geometrically accurate, two-dimensional, sidewall description, with a view to identifying potential shortcomings in the approximate formulations and identifying the physical characteristics that must be accounted for. First, the mean stress state under pressurisation and centrifugal loading is investigated. Finite-Element calculations show that, while the loaded sidewall shape remains close to a toroid, its in-plane tensions differ appreciably from the associated analytical solution. This is largely due to the inability of the anisotropic sidewall material to sustain significant azimuthal stress. An approximate analysis, based on the meridional tension alone, is therefore developed, and shown to yield accurate predictions. In conjunction with a set of formulae for the ‘engineering constants’ of the sidewall material, the approximate solutions provide a straightforward and efficient means of determining the base state for the vibration analysis. The latter is implemented via a ‘waveguide’ discretisation of a variational formulation. Its results show that, while the full geometrical description is necessary for a complete and reliable characterisation of the sidewall’s vibrational properties, a one-dimensional approximation will often be satisfactory in practice. Meridional thickness variations only become important at higher frequencies (above 500Hz for the example considered here), and rotational inertia effects appear to be minor at practical vehicle speeds.

Keywords: road noise, tyre vibration, tyre model

1. Introduction

Noise generated by rolling vehicle tyres is a topic of significant, and growing, concern. From a societal viewpoint, the exterior component represents an environmental pollutant, while its interior counterpart poses a problem for vehicle manufacturers. In both cases, accurate and effective models of the tyre’s vibration characteristics are needed to improve design capabilities.

The obvious approach is the Finite-Element (FE) method. Particular mention here should be given to ‘waveguide’ FE [1], which reduces computational requirements substantially by taking advantage of the tyre’s azimuthal symmetry. However, Lecomte *et al* [2] have argued that there is also a rôle for simpler formulations with even lower costs. A number of such formulations have been proposed; all have in common the representation of the tyre belt by a tensioned plate of some sort. The restoring forces provided by the sidewalls, however, are treated in varying ways. Kropp and co-workers (see, for example, [3], [4]) employ a distributed spring bedding to account for their effect, while Lecomte *et al* [2] model them explicitly, but only in a one-dimensional sense.

An intermediate approach is taken by Pinnington [5], who treats the sidewall as a one-dimensional beam in order to derive equivalent impedances for a set of assumed cross-belt mode shapes.

While the details of the sidewall representation are probably not crucial to accurate modelling of the exterior noise problem, it is likely that they do matter for the structure-borne component of the interior noise (since the sidewalls are part of the transmission path). In this case, one can query the validity of all the approaches taken to date; even Lecomte *et al*'s formulation, while faithful to the tyre cross-sectional geometry, neglects any azimuthal influence on the sidewall properties. The argument for doing so is based on the anisotropy of the sidewall, whose radial reinforcement allows it to sustain a much greater tension in the meridional direction than the azimuthal. There is, however, still a geometrical stiffening effect associated with the sidewall's toroidal shape, and this might be significant, particularly for vibrations at low azimuthal orders. In addition, the azimuthal impedance that the sidewall presents to the belt is unavailable from the one-dimensional formulation. Both these points suggest that a geometrically accurate, two-dimensional representation of the sidewall surface may be necessary. The current work aims to resolve this question.

There are two aspects to be addressed: the stresses and associated displacements due to the steady loading (pressurisation and centrifugal forces), and the characteristics of oscillatory motions about this mean state. Both will be considered in this paper. The steady problem is first attacked with an FE calculation, described in Section 2. The results confirm the expectation of negligible azimuthal tension, and an approximate analytical approach is thus developed on this basis in Section 3. The availability of analytical approximations frees the method from dependence on FE calculations, as long as the 'engineering constants' of the sidewall are known. These parameters are only specified implicitly in the FE model, so in Section 4 they are first extracted, and then compared against candidate formulae for their explicit evaluation.

Sections 5–7 address the dynamical problem. The theoretical approach is set out in Section 5, and verified in Section 6. It is then applied to investigate the importance of accurate representation of the sidewall geometry, both in terms of its toroidal mean surface and its varying thickness. The influence of inertial terms associated with rotation is also studied. The results are presented and discussed in Section 7.

2. Finite-Element calculations

In this section, the FE analysis of the sidewall response to pressurisation is presented. First, the unloaded geometry is introduced, and its discretisation described. Then, in Section 2.3, the representation of the sidewall material is specified. The test cases chosen are set out in Section 2.4, and the results are presented in Section 2.5. The calculations were carried out with the commercial Abaqus FEA software package (version 6.11).¹

2.1. Sidewall geometry

The unloaded sidewall is represented as a (partial) torus, as shown schematically in Fig. 1. The torus has inner radius R_r , outer radius R_b , and height H_s when viewed from the side (i.e. along its axis). In cross-section (the meridional plane), the surface is an arc of radius $R_s^{(0)}$, with its inner end offset by a distance d_r . Cartesian coordinate axes are defined with z in the axial direction, x

¹www.3ds.com/products/simulia/portfolio

horizontal and y vertical. The rectangular polar set (r, θ, z) has azimuthal angle increasing from the x axis according to conventional, right-hand-screw, rotation about the z axis.

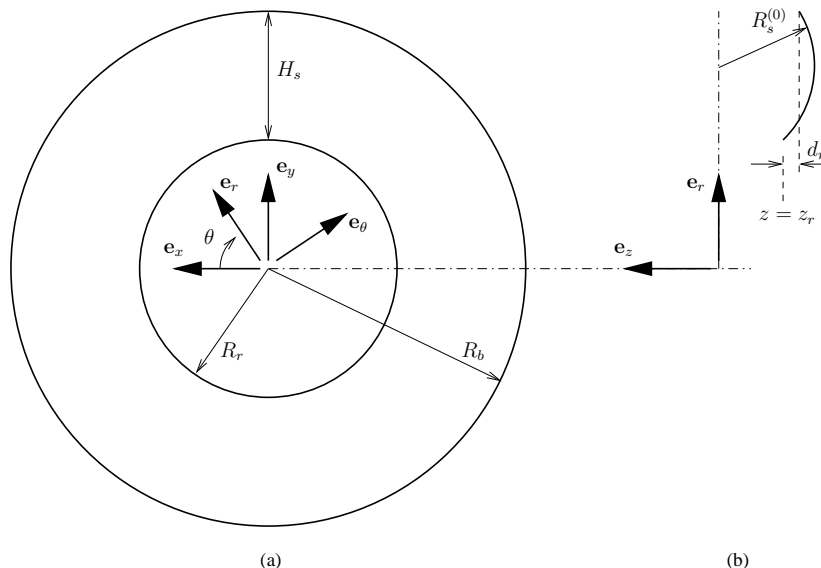


Figure 1: The unloaded sidewall geometry: (a) side view; (b) cross-sectional view. The shape is toroidal, with circular edges of radius R_r and R_b . The inner edge is offset from the outer by a distance d_r , and the cross-sectional arc radius is $R_s^{(0)}$. Cartesian and rectangular-polar coordinate systems are defined by their respective unit vectors.

The geometric parameters introduced above are sufficient to specify the toroidal representation of the unloaded sidewall unambiguously. However, it will subsequently be necessary to refer directly to the z coordinate of the inner edge; this is denoted z_r .

2.2. Mesh and elements

A natural discretisation of the toroidal geometry, yielding quadrilateral elements, is one with constant angular resolution in both azimuthal and meridional directions. This was implemented via a bespoke mesh generator. Fig. 2 shows an example, consisting of 100 (azimuthal) \times 10 (meridional) elements.

In its structural behaviour, the sidewall is to be modelled as a membrane. Therefore the Abaqus FEA element type M3D4 was used. The shape functions for this element are linear.

2.3. Material properties

Two approaches to modelling anisotropic constructions such as a tyre sidewall are available within Abaqus FEA: the ‘engineering constants’ and ‘rebar’ methods. The former, however, is unreliable when the anisotropy is significant, as is the case here. Therefore the ‘rebar’ approach, whereby the stiffening fibres in a composite construction are represented explicitly, was adopted. In this method, the matrix of the reinforced composite is modelled as an isotropic material, and the fibres by an embedded, ‘equivalent’, layer whose thickness is determined by matching the overall fibre cross-sectional area in the plane perpendicular to the reinforcement direction. The Young’s modulus of this layer can be specified, but not its Poisson’s ratio; instead the fibres are assumed incompressible.

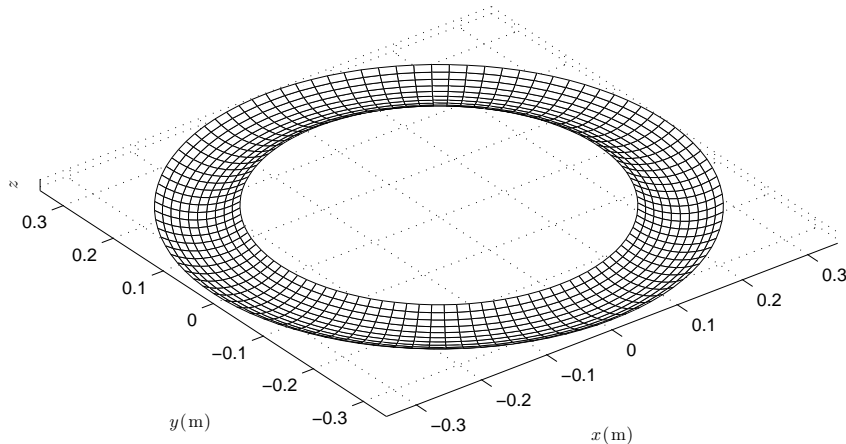


Figure 2: Finite-Element mesh topology. This (low-resolution) example consists of 100 (azimuthal) \times 10 (meridional) quadrilateral elements, with uniform angular spacing in each direction.

Representative parameter values for a tyre sidewall were obtained from sources in the open literature. For the rubber matrix, the Poisson’s ratio is widely accepted to be 0.5, but the Young’s modulus varies not only between compounds, but also with frequency. For the steady loading considered here, the ‘static’ value is required; typical values for rubber compounds used in passenger car tyres are quoted in Table 10.3 of Ref. [6]². In particular, figures of 2.3MPa and 1.2MPa are given for ‘sidewall’ and ‘white sidewall’ respectively. For the current work, a value of 2MPa is used.

Sidewall reinforcing cords can be made from a number of materials, one of which is polyester. Miller *et al* [7] describe a two-ply polyester carcass with 600 cords per metre in each layer, each cord developing 10N force at 1% strain. When combined with Tabaddor *et al*’s [8] quoted Young’s modulus for polyester cord — 4GPa — these figures imply a single cord area of 0.25mm². The fibre spacing was specified in angular terms, at 0.162°, corresponding to 1200 cords per metre at a radius of 294mm.

Although this part of the paper is concerned with static loading of the sidewall, the inclusion of centrifugal effects (see Section 2.4) requires knowledge of its mass. This parameter is available directly from the thicknesses of the matrix and the equivalent reinforcement layer, and their densities. Drawing on Ref. [6], values of 1100kgm⁻³ for rubber, and 1400kgm⁻³ for polyester, were used.

2.4. Test cases

Three test cases, representing successive increases in physical complexity, were chosen. All were based on the Goodyear Wrangler geometry [2], whose salient parameters are repeated here in Table 1. (Note that the belt radius is to be interpreted as that in the pressurised state.) The pressure for each case was set at 2.2 bar (220kPa).

The first test case consists of a stationary sidewall of uniform thickness equal to the average measured on the Wrangler model: 7.5mm. The thickness of the rubber matrix was deduced by subtracting that of the equivalent reinforcement layer from the overall value. Note that this implies

²Available in digital form at books.google.com

Belt radius, R_b [m]	0.346
Sidewall height, H_s [m]	0.104
Sidewall rim displacement, d_r [m]	0.002

Table 1: Geometrical parameters for the Goodyear Wrangler tyre

a slight variation with radial distance from the tyre axis, due to the uniform angular separation of constant-area reinforcing cords. At the mean radius of 294mm, the rubber thickness is 7.2mm.

The second test case introduces rotation about the tyre axis, which results in an additional, steady, centrifugal loading. An angular velocity of 104rads^{-1} , corresponding to a vehicle speed of 130 kilometres per hour, was chosen. While this would, in reality, increase the circumferential strain in the belt (by approximately one-third), the radius is here held fixed so that direct comparison is possible.

Finally, the mass dependence implicit in the centrifugal loading component raises the question of how sidewall thickness variations affect the results. This is addressed via the third test case, which uses the measured thickness distribution for the Wrangler tyre [2], repeated here in Table 2.

l [mm]	0	5	15	25	35	45	55	65	75	85	95	105	110
h_s [mm]	15	13	10	8	7	6.5	6	6.5	6.5	7	7	9	10

Table 2: Measured sidewall thickness, h_s , as a function of arc length, l .

2.5. Results

Although the component materials are specified as linear elastic, the calculation is non-linear in a geometric sense; i.e. the final stress state is in equilibrium for the strained, rather than original, geometry. This requires an iterative calculation, which is handled automatically by the software package. Zero-displacement boundary conditions were specified at the membrane edges. A mesh of 500×50 elements was employed; convergence checks against the results for a 250×25 discretisation showed a worst-case deviation in the boundary meridional tension of 0.20%. No departures from the expected axisymmetry were observed.

2.5.1. Pressurised sidewall shape

Fig. 3 shows the inflated sidewall shapes for the three test cases — uniform stationary, uniform rotating and non-uniform rotating — with the original shape also plotted for comparison. The stretched arc length is very similar between cases, corresponding to extensions of 1.742mm, 1.755mm and 1.751mm on the original 110mm. While these values are relatively small, the associated change in shape is significant. This can be demonstrated by considering the radii of ‘equivalent’ circular arcs, defined by the rim point, the hub point and the stretched length. These arcs are also plotted in Fig. 3, and have radii 85.85mm, 85.79mm and 85.81mm, compared to 95.50mm for the unstretched geometry. Such changes provide *post hoc* justification for the specification of a geometrically non-linear calculation.

The equivalent arcs also provide a useful reference for assessing the stretched shapes. In the uniform stationary case, the two are very close, with the pressurised sidewall having a relative displacement in the radial direction. This arises because of the growing size of (and hence pressure

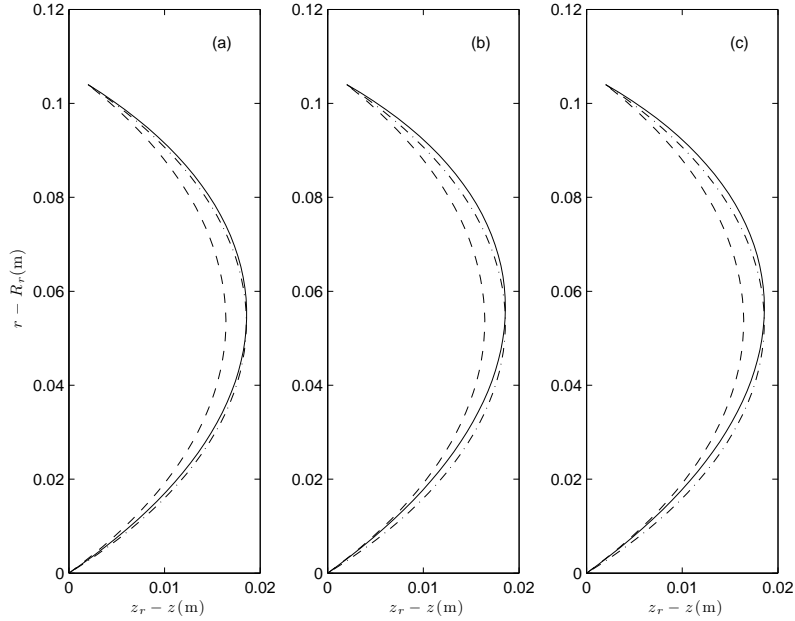


Figure 3: Loaded sidewall shapes for: (a) uniform thickness, non-rotating; (b) uniform thickness, rotating; and (c) varying thickness, rotating cases. Included for comparison are the unloaded shape (---) and the ‘equivalent circular arc’ with length equal to the loaded shape (— · —). Axes are chosen for consistency with the cross-sectional view in Fig. 1(b).

forces on) azimuthal rings as the radial distance increases. On the addition of (radially acting) centrifugal forces due to rotation, the relative displacement increases, but the subsequent effect of changing the thickness distribution is not discernible in Fig. 3.

2.5.2. In-plane tensions

The vibrational properties of the sidewall depend crucially on its in-plane tensions. These parameters were derived from the FE output for the reinforcement tension and the rubber stresses (taking thickness reduction due to strain into account). To aid in their consideration, an angular variable ϕ is defined, on the basis of the equivalent circular arc (Fig. 4). If $s_2 - s_{20}$ is the distance around the (equivalent or real) arc from the rim point, then $\phi = (s_2 - s_{20})/R_s$, where R_s is the equivalent arc radius. The offset s_{20} is chosen so that $\phi = 0$ at the point on the equivalent arc with purely radial tangent.

Fig. 5 shows the azimuthal and meridional tensions for the stationary case. Immediately evident is the influence of the (strong) anisotropy; the azimuthal tension is two orders of magnitude lower than the meridional. This is because the (meridional) reinforcing fibres effectively also stiffen the azimuthal direction via the directional coupling inherent in the toroidal geometry. Azimuthal stretching cannot occur without concomitant meridional extension, which is limited by the reinforcement. As a result, the meridional and azimuthal strains are of similar magnitude; the in-plane tensions then reflect the difference in effective modulus between the two directions.

This point is further emphasised by considering the in-plane tensions for the toroidal membrane defined by the equivalent circular arc. These are given by, for example, Timoshenko and Woinowsky-Krieger ([9], Ch.14) as:

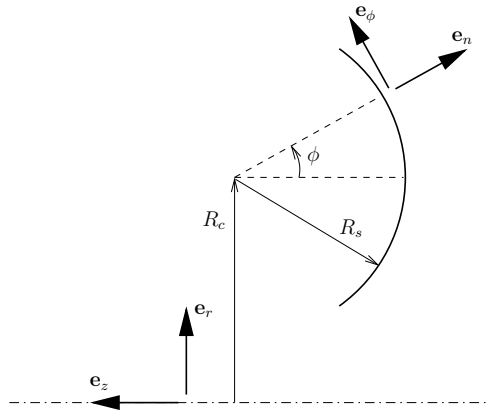


Figure 4: Local coordinate system based on the equivalent circular arc (of radius R_s .) The parameter R_c is the distance from the tyre axis to the arc's centre.

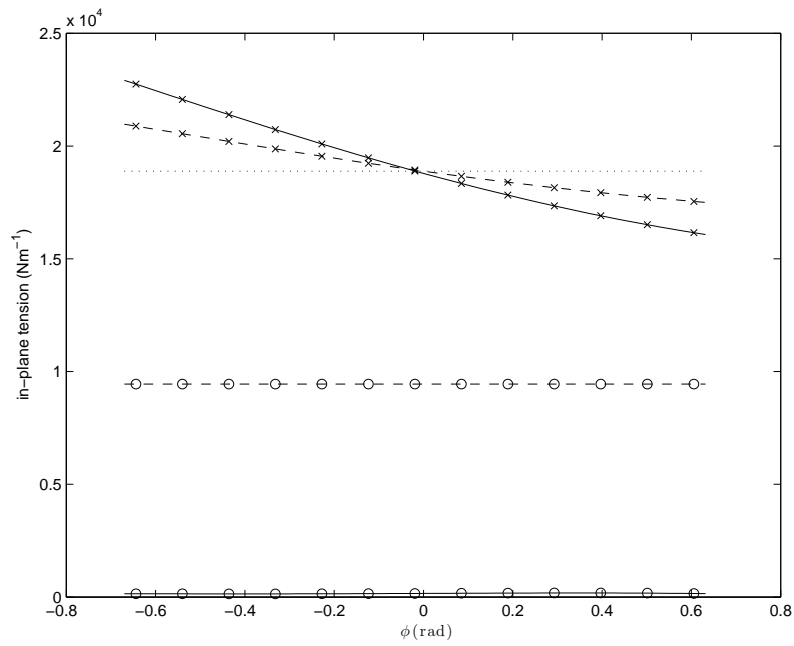


Figure 5: In-plane tensions for the non-rotating case: —, FE calculation; --, analytical solution for torus. Azimuthal components are indicated by circular markers, and meridional by crosses. Also shown is a dotted line at the value of pR_s .

$$N_{11} = \frac{pR_s}{2}, \quad N_{22} = \frac{pR_s}{2} \frac{2R_c + R_s \sin \phi}{R_c + R_s \sin \phi}, \quad (1)$$

where index 1 represents the azimuthal direction, index 2 the meridional, and R_c is the radial position of the meridional centre of curvature (see Fig. 4). These expressions are self-evidently of comparable magnitude, as is confirmed by their values for the current case (included in Fig. 5). As a result, the azimuthal tension represents a gross over-estimate of the corresponding parameter in a tyre sidewall. The meridional expression does at least give values comparable with the FE results, but its accuracy cannot be described as satisfactory.

Finally, Fig. 5 also shows, as a dotted line, the constant value pR_s that would apply for the one-dimensional, circular-arc, case (i.e. where the geometry of Fig. 4 is simply extended perpendicular to the drawing plane). Given the negligible azimuthal tension, one might expect the meridional tension to be well approximated by this value. In fact, it is even less successful than the toroidal form of Eq. (1). A more careful representation of the pressurised geometry is clearly necessary.

The influences of rotation and thickness non-uniformity on the meridional tension are shown by Fig. 6, which presents the results for all three test cases. Departures from the one-dimensional value, pR_s , are increased by centrifugal effects, but the differences between the uniform- and variable-thickness sidewalls are small.

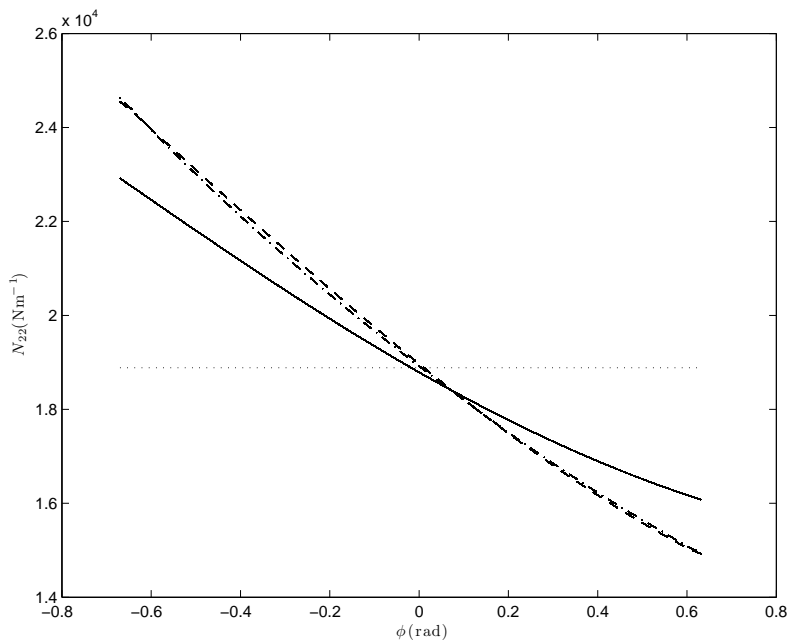


Figure 6: Meridional tensions for: —, non-rotating case; --, uniform-thickness rotating case; -·-, varying thickness rotating case. Dotted line at pR_s .

3. Analytical approximations

The results of the FE calculations suggest that the most obvious potential approximations to the pressurised sidewall geometry — the one-dimensional circular arc and the two-dimensional toroidal

surface — are unlikely to form a satisfactory basis for a vibration analysis. Equally, however, the displacement and stress fields remain simple enough that it may be possible to describe them analytically. This would eliminate the need for a fresh FE computation for each parameter set in a design process, with clear efficiency benefits.

The approach presented here is based on a perturbation analysis, with the pressurised sidewall shape regarded as a small modification to the equivalent circular arc geometry introduced previously. This representation admits an asymptotic solution, which will be seen to compare well with the FE results. The issue of its application in the absence of any FE data will also be discussed.

3.1. The perturbation approach

The equivalent circular arc is shown in Fig. 4. In addition to its radius R_s , it is defined by (cf. also Fig. 1) the rim and belt radii, R_r and R_b , and the rim axial offset, d_r . Derived parameters, in terms of which the analysis is more concise, are the radial coordinate of the meridional centre of curvature, R_c , and the limiting values of the angle ϕ : $\phi = -\phi_r$ at the rim and $\phi = \phi_b$ at the belt. Finally, it is also convenient to introduce local basis vectors \mathbf{e}_ϕ and \mathbf{e}_n , related to \mathbf{e}_r and \mathbf{e}_z as follows:

$$\mathbf{e}_\phi = \mathbf{e}_r \cos \phi + \mathbf{e}_z \sin \phi; \quad \mathbf{e}_n = \mathbf{e}_r \sin \phi - \mathbf{e}_z \cos \phi. \quad (2)$$

The set $(\mathbf{e}_\theta, \mathbf{e}_\phi, \mathbf{e}_n)$ forms an orthogonal, right-handed basis, with \mathbf{e}_θ and \mathbf{e}_ϕ lying in the toroidal surface specified by the circular arc, and \mathbf{e}_n perpendicular to it.

The pressurised sidewall shape is now expressed in terms of its displacement \mathbf{w} from the circular arc, with

$$\mathbf{w}(\phi) = w_\phi(\phi)\mathbf{e}_\phi + w_n(\phi)\mathbf{e}_n. \quad (3)$$

On the basis of the examples shown in Fig. 3, it is assumed that this displacement represents a small perturbation to the circular arc, i.e. $|\mathbf{w}|/R_s \ll 1$.

3.2. The equilibrium equations

To consider the equilibrium of the pressurised sidewall, its shape must be characterised further. First, two appropriate coordinates, which can be used to specify position on the surface, must be chosen. Then the associated ‘metric coefficients’, α_1 and α_2 , must be found. Finally, the principal curvatures are also required. As part of this process, local unit basis vectors $(\mathbf{e}_1, \mathbf{e}_2, \mathbf{e}_3)$, with \mathbf{e}_1 and \mathbf{e}_2 tangent to the surface and \mathbf{e}_3 perpendicular, are automatically identified. A full derivation of these parameters can be found in Ref. [10]. The key results for the current application can briefly be summarised as follows.

According to the definition of the circular arc and the perturbation displacement, the surface is described by the position vector

$$\mathbf{r} = R_c \mathbf{e}_r + (R_s + w_n) \mathbf{e}_n + w_\phi \mathbf{e}_\phi. \quad (4)$$

A natural choice of coordinates is (θ, ϕ) , whereupon α_1 , α_2 and \mathbf{e}_1 , \mathbf{e}_2 are defined via:

$$\alpha_1 \mathbf{e}_1 = \frac{\partial \mathbf{r}}{\partial \theta}, \quad \alpha_2 \mathbf{e}_2 = \frac{\partial \mathbf{r}}{\partial \phi}. \quad (5)$$

(In the absence of displacement, this would yield $\mathbf{e}_1 = \mathbf{e}_\theta$ and $\mathbf{e}_2 = \mathbf{e}_\phi$. With displacement, the latter equality is lost, although it will remain approximately true for the small perturbations envisaged.) The perpendicular vector \mathbf{e}_3 (corresponding approximately to \mathbf{e}_n) follows from the vector product of \mathbf{e}_1 and \mathbf{e}_2 . Finally, the principal curvature of interest is

$$\kappa_2 = -\frac{\partial^2 \mathbf{r}}{\partial s_2^2} \cdot \mathbf{e}_3, \quad (6)$$

where s_2 is, as previously, the distance along the sidewall in the meridional plane.

The general equilibrium equations for a membrane surface are given by Soedel [11, Section 11.3]. They simplify considerably for the current, axisymmetric problem, and can be further reduced by neglecting the (small) azimuthal tension. The resulting expressions are:

$$\frac{d}{d\phi} (\alpha_1 N_{22}) = -M\Omega^2 \alpha_1^2 \alpha_2 \mathbf{e}_r \cdot \mathbf{e}_2, \quad (7)$$

$$\kappa_2 N_{22} = p + M\Omega^2 \alpha_1 \mathbf{e}_r \cdot \mathbf{e}_3, \quad (8)$$

in which p is the inflation pressure, M the sidewall mass per unit area, and Ω the wheel's angular velocity. These are to be solved for the meridional tension, N_{22} , and the perturbation displacements w_ϕ , w_n (which implicitly define the surface's geometric parameters).

It has not been possible to find an exact solution. However, approximate formulae have been obtained via an asymptotic approach. The details of the analysis are set out in Appendix A. The results are:

$$w_\phi \simeq \frac{R_s^2 + 2\mu^{(0)} R_c^2}{24R_c} (\phi + \phi_r)^2 (\phi - \phi_b)^2, \quad (9)$$

$$w_n \simeq -\frac{R_s^2 + 2\mu^{(0)} R_c^2}{12R_c} (\phi + \phi_r) (\phi - \phi_b) (2\phi + \phi_r - \phi_b), \quad (10)$$

$$N_{22} \simeq p \frac{R_s R_c}{\alpha_1} \left[1 - \left(\frac{R_s}{R_c} + 2\mu^{(0)} \frac{R_c}{R_s} \right) \frac{\phi_r - \phi_b}{2} - \mu^{(0)} \frac{R_c}{R_s} \phi \right]. \quad (11)$$

In these expressions, α_1 is taken as equal to its approximate form, $R_c + R_s \sin \phi$, and $\mu^{(0)}$ is the constant coefficient of a polynomial expansion (in ϕ) of the dimensionless centrifugal force parameter,

$$\mu = \frac{M\Omega^2 R_s}{p}. \quad (12)$$

3.3. Comparison with FE results

Fig. 7 shows the perturbation displacements for the stationary case. Both the qualitative form and the values of the numerical results are very well represented by the approximate expressions. In absolute terms, the agreement is better for w_ϕ , but the relative errors are comparable between the two components.

The corresponding plots for the rotating cases are given in Figs. 8 (uniform thickness) and 9 (varying thickness). The curves are very similar in form to those for the non-rotating case, but have approximately doubled in magnitude. The approximate formulae are still successful, albeit

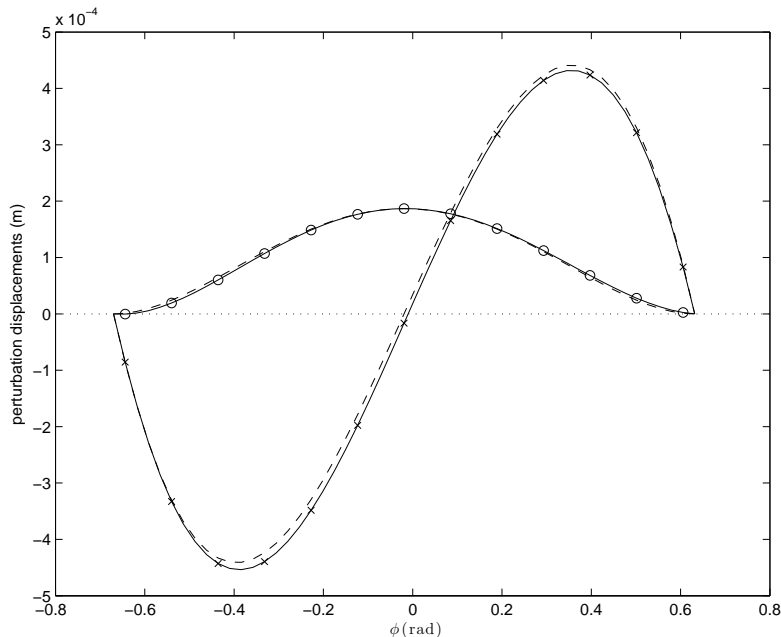


Figure 7: Displacements relative to equivalent circular arc for non-rotating case: —, FE calculation; - -, approximate solution. Circular markers indicate tangential component, w_ϕ ; crosses normal component, w_n .

with reduced accuracy; they also show a greater influence of thickness variation than the numerical results. In fact, it could be argued that the uniform-thickness approximations would be better than their varying-thickness counterparts in the latter case, i.e. that $\mu^{(0)}$ in Eqs. (9) and (10) should be replaced by the mean value of μ . This has not been done for two reasons: first, because it would be questionable to make such an *ad hoc* modification without further supporting evidence; and second, because the most important parameter for subsequent vibration calculations will be the meridional tension.

This quantity is considered in Fig. 10, which shows the comparisons between the FE and approximate solutions for all three test cases. All are excellent (note the use of a false y -axis origin to enhance plot resolution), although the pattern of worsening accuracy with the inclusion of rotational effects carries over from the displacement results. An important difference, however, is that the approximation for the uniform-thickness rotating case is not obviously superior to that for varying thickness, justifying the retention of the asymptotic formulae in their original form.

3.4. Application considerations

The results of the previous section demonstrate the validity of using the analytical approximations in place of an FE calculation for the mean stress state. The analysis presented so far is, however, incomplete for this purpose, because the theoretical formulae have been evaluated on the basis of the stretched arc length provided by the FE. A fully independent method requires knowledge of the elastic constants linking in-plane tensions and strains. Unfortunately, the material specification used in the FE calculation provides only an implicit definition of these constants. The derivation of an explicit representation is the topic of the next section.

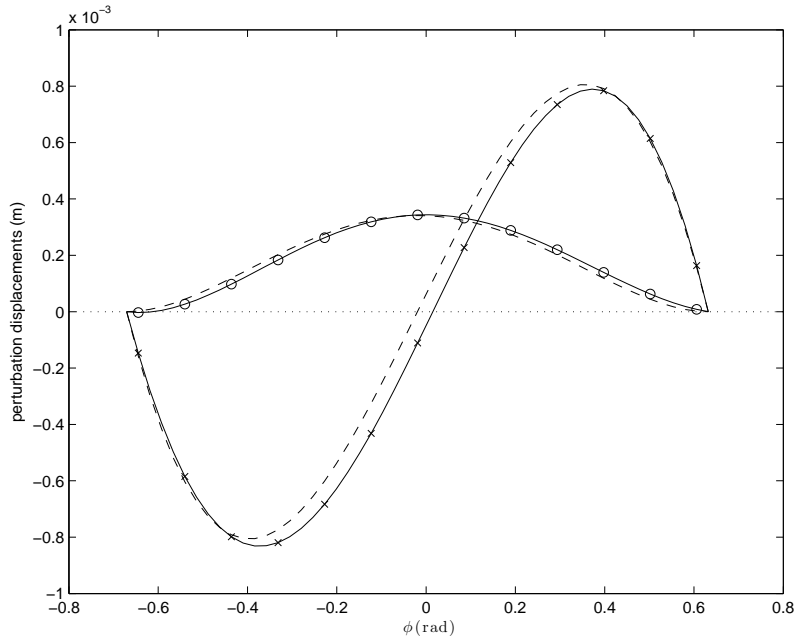


Figure 8: Displacements relative to equivalent circular arc for uniform-thickness rotating case: —, FE calculation; --, approximate solution. Circular markers indicate tangential component, w_ϕ ; crosses normal component, w_n .

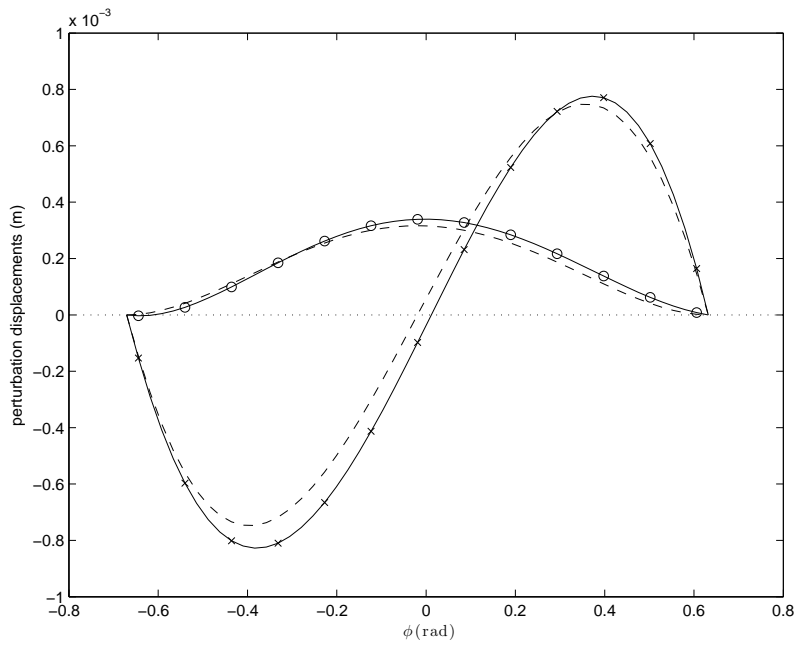


Figure 9: Displacements relative to equivalent circular arc for varying thickness rotating case: —, FE calculation; --, approximate solution. Circular markers indicate tangential component, w_ϕ ; crosses normal component, w_n .

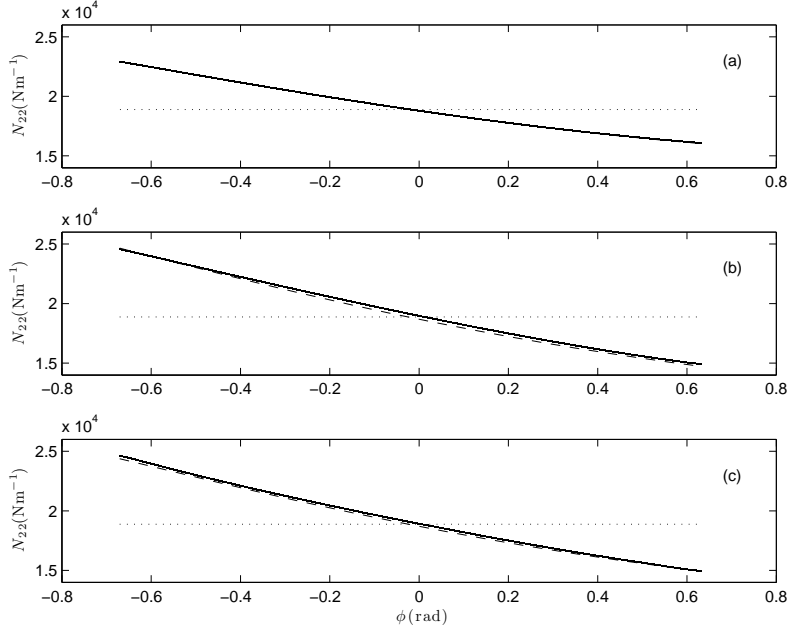


Figure 10: Meridional tensions for (a) uniform-thickness, non-rotating; (b) uniform-thickness, rotating; and (c) varying thickness, rotating cases. Comparisons are between FE results (—) and analytical approximations (---). Dotted lines at pR_s .

4. Engineering constants for the sidewall material

4.1. The engineering constants formulation

The ‘engineering constants’ of an anisotropic material are the Young’s moduli and Poisson’s ratios measurable in uni-axial tension/compression, and the shear moduli. For a composite lamina, in a state of plane stress, five such constants enter into the ‘compliance matrix’, which links stresses to strains as follows:

$$\begin{bmatrix} \epsilon_1 \\ \epsilon_2 \\ \gamma_{12} \end{bmatrix} = \begin{bmatrix} 1/E_1 & -\nu_{21}/E_2 & 0 \\ -\nu_{12}/E_1 & 1/E_2 & 0 \\ 0 & 0 & 1/G_{12} \end{bmatrix} \begin{bmatrix} \sigma_1 \\ \sigma_2 \\ \tau_{12} \end{bmatrix} \quad (13)$$

(see, for example, Section 5.2 of Ref. [12]). Here the subscripts ‘1’ and ‘2’ represent orthogonal in-plane directions; σ_1 and σ_2 are the normal stresses and τ_{12} the shear. With η_1 and η_2 as coordinates in the 1 and 2 directions, the strains are given in terms of the displacements u_1 and u_2 as

$$\epsilon_1 = \frac{\partial u_1}{\partial \eta_1}, \quad \epsilon_2 = \frac{\partial u_2}{\partial \eta_2}, \quad \gamma_{12} = \frac{\partial u_2}{\partial \eta_1} + \frac{\partial u_1}{\partial \eta_2}. \quad (14)$$

The compliance matrix is symmetrical, implying that

$$\frac{\nu_{21}}{E_2} = \frac{\nu_{12}}{E_1}. \quad (15)$$

Hence only four of the five constants introduced in Eq. (13) are independent.

4.2. Determination of the engineering constants

The engineering constants for a constant reinforcement spacing can be found by subjecting a rectangular geometry to a series of FE ‘tests’. These are shown schematically in Fig. 11. In the first two, the strain is uniaxial (i.e. $\epsilon_x = \epsilon$, $\epsilon_y = 0$ and $\epsilon_x = 0$, $\epsilon_y = \epsilon$). In the last, equal and opposite strains are applied in the x and y directions in order to generate a state of pure shear in an axis system rotated by 45° . The reinforcement direction in each case is indicated by the lines inside the rectangles.

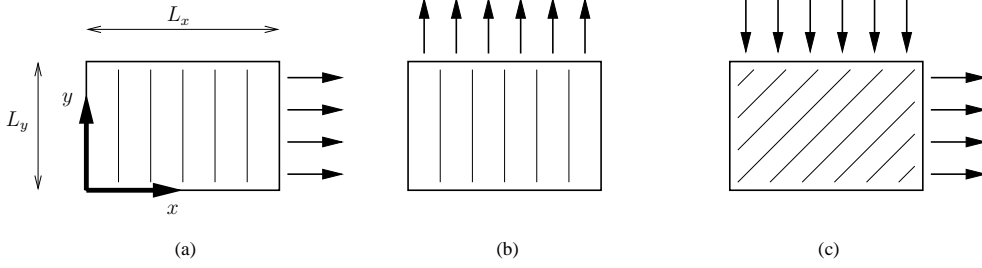


Figure 11: Rectangular membrane test cases for extraction of engineering constants from the FE material representation: (a) pure longitudinal strain; (b) pure lateral strain; and (c) pure shear strain on $45^\circ/135^\circ$ planes. Lines inside rectangles indicate the reinforcement direction for each case.

In all cases, for consistency with the sidewall application, the ‘2’ direction was taken parallel to the reinforcement. Thus, in cases (a) and (b), (1,2) correspond directly to (x, y) , while in case (c) they are rotated 45° clockwise. For each, the compliance equations are easily inverted, yielding

$$\begin{pmatrix} \sigma_x \\ \epsilon_x \end{pmatrix}_a = \frac{E_1}{1 - \nu_{12}\nu_{21}}, \quad \begin{pmatrix} \sigma_y \\ \epsilon_x \end{pmatrix}_a = \frac{\nu_{12}E_2}{1 - \nu_{12}\nu_{21}}; \quad (16)$$

$$\begin{pmatrix} \sigma_x \\ \epsilon_y \end{pmatrix}_b = \frac{\nu_{21}E_1}{1 - \nu_{12}\nu_{21}}, \quad \begin{pmatrix} \sigma_y \\ \epsilon_y \end{pmatrix}_b = \frac{E_2}{1 - \nu_{12}\nu_{21}}; \quad (17)$$

$$\frac{1}{2} \begin{pmatrix} \sigma_y - \sigma_x \\ \epsilon_y - \epsilon_x \end{pmatrix}_c = G_{12}. \quad (18)$$

(Standard axis transformation formulae have been used for τ_{12} and γ_{12} in order to obtain the final result.) The FE tests yield the five stress-strain ratios in these expressions, allowing the elastic constants to be found as follows:

$$\nu_{12} = \frac{(\sigma_y/\epsilon_x)_a}{(\sigma_y/\epsilon_y)_b}, \quad \nu_{21} = \frac{(\sigma_x/\epsilon_y)_b}{(\sigma_x/\epsilon_x)_a}; \quad (19)$$

$$E_1 = (1 - \nu_{12}\nu_{21}) \begin{pmatrix} \sigma_x \\ \epsilon_x \end{pmatrix}_a, \quad E_2 = (1 - \nu_{12}\nu_{21}) \begin{pmatrix} \sigma_y \\ \epsilon_y \end{pmatrix}_b. \quad (20)$$

The shear modulus is, of course, already given explicitly.

The FE analysis of the test cases in Fig. 11 was carried out with $L_x = 1.316\text{m}$, $L_y = 1\text{m}$, and a reference strain of 0.1%. The associated boundary conditions are summarised in Table 3. The same, rectangular, membrane elements as for the sidewall analysis were used; a mesh of 49×37 provided comfortably enough resolution for numerical accuracy (agreement to 5 digits with

26 × 20 results). The matrix and reinforcing elements were given the material properties specified in Section 2.3, with dimensions corresponding to the uniform-thickness sidewall at radius 294mm, i.e. rubber thickness 7.2mm, cord area 0.25mm² and spacing 0.833mm (giving an equivalent layer thickness of 0.3mm). Geometrical non-linearity was not included. (The fully linear nature of the calculation was checked and confirmed by running the reverse of case (c).) The overall stresses were deduced from the calculated reaction forces at the edge nodes. The associated engineering constants are given in Table 4, in the following section.

Case	$x = 0$	$y = 0$	$x = L_x$	$y = L_y$
(a)	$u_x = u_y = 0$	$u_y = 0$	$u_x = 1.316 \times 10^{-3}, u_y = 0$	$u_y = 0$
(b)	$u_x = 0$	$u_x = u_y = 0$	$u_x = 0$	$u_x = 0, u_y = 1 \times 10^{-3}$
(c)	$u_x = 0$	$u_y = 0$	$u_x = 1.316 \times 10^{-3}$	$u_y = -1 \times 10^{-3}$

Table 3: Boundary conditions for the FE test cases in Fig. 11. The variables u_x, u_y are the displacements in the x and y directions, and all values are in metres.

4.3. Approximate expressions for the engineering constants

The engineering constants derived from the FE tests are listed in the first column of Table 4. One point can immediately be noted: the shear modulus is very close to that of the rubber matrix, $G = 0.667\text{MPa}$. It is, in fact, equal to $V_r G_r$, where V_r is the rubber volume fraction (0.96). This result is intuitively plausible, if one accepts that the FE analysis treats the reinforcing cords as having no shear stiffness. Thus,

$$G_{12} = V_r \frac{E_r}{2(1 + \nu_r)}, \quad (21)$$

where E_r and ν_r are the Young's modulus and Poisson's ratio for the rubber. That this result is not simply a numerical coincidence has been confirmed by checks against a number of other parameter sets.

A natural starting point in attempting to predict the other elastic constants is the set of well-known 'mixture rule' formulae (see, for example, Ref. [12]):

$$E_1 = \left(\frac{V_c}{E_c} + \frac{V_r}{E_r} \right)^{-1} \quad (22)$$

$$E_2 = V_c E_c + V_r E_r; \quad (23)$$

	FE	MR	HT	Current
$E_1(\text{MPa})$	2.55	2.08	2.25	2.66
$E_2(\text{MPa})$	162	162	162	162
ν_{21}	0.500	0.500	0.500	0.500
$G_{12}(\text{MPa})$	0.640	–	0.615–0.722	0.667

Table 4: Engineering constants for the sample parameter set. FE: from Finite-Element tests; MR: from the 'mixture rule', Eqs. (22)-(24); HT: from the Halpin-Tsai formulae, Eqs. (23)-(26); Current: Eqs. (23), (24), (35), (36).

$$\nu_{21} = V_c \nu_c + V_r \nu_r. \quad (24)$$

(Here E_c , ν_c and $V_c = 1 - V_r$ are the Young's modulus, Poisson's ratio and volume fraction of the cord material. Note that the choice of '2' to denote the reinforcement direction means that '1' and '2' are reversed in comparison to the conventional form of these expressions.) The results for the current parameter set are presented in the second column of Table 4. Essentially perfect agreement with the FE values is evident for E_2 and ν_{21} (although it should be recognised that *any* suitably weighted average of ν_c and ν_r would work in this particular case), but the estimate for E_1 is significantly lower. This is consistent with the weaker theoretical basis for Eq. (22) in comparison to Eqs. (23) and (24).

More sophisticated estimates are available from the 'Halpin-Tsai' equations [13], which consist of the mixture-rule expressions for E_2 and ν_{21} , augmented by two further formulae for E_1 and G_{12} :

$$E_1 = E_r \frac{(1 + \alpha_E V_c) E_c + \alpha_E V_r E_r}{V_r E_c + (\alpha_E + V_c) E_r}, \quad (25)$$

$$G_{12} = G_r \frac{(1 + \alpha_G V_c) G_c + \alpha_G V_r G_r}{V_r G_c + (\alpha_G + V_c) G_r}. \quad (26)$$

The constants α_E and α_G are empirically determined, although there is theoretical justification for $\alpha_G = 1$ in the case of a composite with cylindrical reinforcing fibres [13]. For the cord-rubber construction of interest here, $\alpha_E = 2$ and $\alpha_G = 1$ appear to be accepted values ([8], [6, Section 3.1]), and these were used to provide the entries in the third column of Table 4. (Due to uncertainty over the shear modulus of the twisted-fibre cord, a range is given for G_{12} , corresponding to variation in G_c from zero to infinity.) The value for E_1 represents an improvement on the mixture rule, but still differs from the FE result by over 10%. The limiting values for G_{12} bracket the corresponding FE result, and represent relative deviations of $-4\%/+13\%$.

Although not excessive by the standards of composite stiffness uncertainty, these discrepancies are undesirable. The following approximate analysis for E_1 was therefore developed.

Consider the application of uniaxial stress in the 1 direction. As in the mixture-rule approach, it is assumed that the stresses (σ_c, σ_r) and strains (ϵ_c, ϵ_r) in the composite components can be characterised by single, average values. Parallel to the cords, the strains are equal:

$$\epsilon_{2c} = \epsilon_{2r} = \epsilon_2, \quad (27)$$

and force equilibrium requires that

$$V_c \sigma_{2c} + V_r \sigma_{2r} = 0. \quad (28)$$

The usual, tenuous, assumption of equal stresses perpendicular to the cords is eschewed; however, the standard expression for the strain, i.e.

$$\epsilon_1 = V_c \epsilon_{1c} + V_r \epsilon_{1r}, \quad (29)$$

is legitimate, and is therefore retained. Finally, Hooke's law for the rubber component in plane stress can be written as

$$E_r \epsilon_{1r} = \sigma_{1r} - \nu_r \sigma_{2r}, \quad (30)$$

$$E_r \epsilon_2 = -\nu_r \sigma_{1r} + \sigma_{2r}. \quad (31)$$

For the typical case of significant stiffening by the reinforcement, the second of these equations implies that the two stress components in the rubber matrix are of comparable magnitude.

To allow further progress, the cord stress in the 1 direction is neglected in comparison to σ_{2c} (on the basis that it will be comparable to the matrix stresses, whereas Eq. (28) implies $\sigma_{2c} \gg \sigma_{2r}$ for a typical reinforcement volume fraction). Hooke's law for the cord is then simply

$$\sigma_{2c} = E_c \epsilon_2, \quad (32)$$

and the cord strain in the 1 direction, ϵ_{1c} , is approximately $-\nu_c \epsilon_2$. In anticipation of a very small secondary Poisson's ratio, $\nu_{12}(= -\epsilon_2/\epsilon_1)$, this implies that the cord contribution to Eq. (29) is negligible, and hence that

$$\epsilon_{1r} = \frac{\epsilon_1}{V_r}. \quad (33)$$

It is now possible to link the overall strains, ϵ_1 and ϵ_2 , by first eliminating σ_{1r} between Eqs. (30) and (31), and then using Eqs. (28), (32) and (33) to substitute for σ_{2r} and ϵ_{1r} . This yields the following expression for the secondary Poisson's ratio, $-\epsilon_2/\epsilon_1$:

$$\nu_{12} = \nu_r \frac{E_r}{E_2 - \nu_r^2 V_c E_c}, \quad (34)$$

in which E_2 is given by the mixture-rule formula, Eq. (23). The transverse Young's modulus follows directly, given the compliance-matrix symmetry condition, Eq. (15), and the mixture rule for ν_{21} , Eq. (24):

$$E_1 = E_r \frac{E_2}{E_2 - \nu_r^2 V_c E_c} \frac{\nu_r}{V_c \nu_c + V_r \nu_r}. \quad (35)$$

This formula appears not to have been derived before. Although approximate, it has the advantage of employing no empirical parameters. Note also that, in the limit of dominant reinforcement stiffness ($V_r E_r / V_c E_c \rightarrow 0$), it is very close to $E_r / (1 - \nu_r^2)$, i.e. the plane-strain modulus for the rubber matrix alone. This is intuitively plausible, as very stiff fibres could be expected to maintain $\epsilon_2 \simeq 0$ in this loading case.

For the current parameters, the estimate arising from Eq. (35) is given in the final column of Table 4. It exceeds the FE value by 4%. This difference is not coincidental; it has been ascertained that the FE results across a range of parameter values always match the current formula scaled by the rubber volume fraction. Had the approximate analysis assumed that $\epsilon_{1r} = \epsilon_1$, instead of ϵ_1/V_r , exact agreement with the FE could have been obtained. However, the resulting formula would be physically invalid in the sense that it could predict $E_1 < E_r$ (consider the dominant-fibre-stiffness case, with $\nu_r = \nu_c$ and $V_r < 1 - \nu_r^2$). Hence the discrepancy represents a fundamental weakness in the FE formulation (albeit one which only becomes significant at higher cord volume fractions), and it is preferable to retain Eq. (35).

In the light of this observation, one should also reconsider Eq. (21) for the shear modulus. The implicit neglect of *any* contribution from the reinforcement is unlikely to be tenable; at a minimum, the shear modulus should not be reduced by its presence. The set of approximations derived here is thus completed by the expression

$$G_{12} = \frac{E_r}{2(1 + \nu_r)}, \quad (36)$$

which, albeit lacking a theoretical basis, is unlikely to be seriously in error. (It differs from the maximum Halpin-Tsai estimate by only 8%.)

To summarise: formulae for the engineering constants of the sidewall material representation employed in the FE analysis of Section 2 have been obtained. They are given by Eqs. (23), (24), (35) and (36), and provide values differing from those implicit in the FE representation by at most 4% (or, in general, a factor V_r^{-1}). The most dominant engineering constant, E_2 , is reproduced effectively exactly. Of the formulae, Eq. (35) appears to be novel.

4.4. Mean stress calculation

We can now return to the issue that motivated this section: establishing the pre-stressed state. To do so, it is necessary to find an equivalent arc radius, R_s , a tension distribution N_{22} (evaluated via Eq. (11)) and an associated strain distribution that are consistent with one another. This is achieved via an iterative calculation. Given an initial estimate for R_s , the strain is evaluated as $N_{22}/(E_2 h_s)_0$, where the ‘0’ subscript indicates the unstressed state. This provides an updated solution for R_s , completing the iteration loop. (Note that this approach employs the nominal stress and strain, unlike the geometrically non-linear FE calculation. Greater sophistication was deemed unnecessary, given the predicted strain values.) Having found the converged solution, the engineering constants for the dynamical analysis are calculated on the basis of the strained geometry, using the relationships set out above.

The efficiency benefit of employing the analytical approximations for the pre-stress calculation is enormous. When implemented in the Matlab (2012a) environment, execution time on a 16-core Linux server ($2 \times$ Intel Xeon L5630 2.13GHz CPUs) was 0.3s. In comparison, the FE calculation took 456s on the same machine.

5. Dynamical analysis

The equations governing the sidewall vibrations are derived using a variational analysis, following the approach taken by Lecomte *et al* [2] for the tyre belt. Here, however, the base geometry is not as simple as the cylindrical belt; it is the deformed torus whose analytical description is given in Appendix A. Auxiliary relations that are useful in the derivation are given in Appendix B. The derivation itself consists of two parts; formulation of the expressions for the energy quantities (Section 5.1), and the variational analysis itself (Section 5.2). Numerical discretisation is most conveniently carried out before variations are taken, and is thus described at the beginning of the latter section.

5.1. Energy quantities

The displacement from the base state is denoted by \mathbf{u} , where

$$\mathbf{u} = u_1 \mathbf{e}_1 + u_2 \mathbf{e}_2 + u_3 \mathbf{e}_3, \quad (37)$$

with \mathbf{e}_1 ($= \mathbf{e}_\theta$), \mathbf{e}_2 ($\approx \mathbf{e}_\phi$) and \mathbf{e}_3 ($\approx \mathbf{e}_n$) the azimuthal, meridional and normal vectors defined in Section 3.2. Hence the kinetic energy of the sidewall is given by

$$T = \frac{1}{2} \int_{-\phi_r}^{\phi_b} \int_0^{2\pi} M \left| \alpha_1 \Omega \mathbf{e}_1 + \frac{\partial \mathbf{u}}{\partial t} \right|^2 \alpha_1 \alpha_2 d\theta d\phi, \quad (38)$$

The potential energy is given by the sum of three contributions:

$$U = U_s + U_p + U_a, \quad (39)$$

in which U_s , U_p and U_a are the contributions from perturbation strains, pre-stress and cavity pressure respectively. The first has the standard form

$$U_s = \frac{1}{2} \int_{-\phi_r}^{\phi_b} \int_0^{2\pi} [A_{11}\epsilon_{11}^2 + 2A_{12}\epsilon_{11}\epsilon_{22} + A_{22}\epsilon_{22}^2 + A_{66}\gamma_{12}^2] \alpha_1\alpha_2 d\theta d\phi, \quad (40)$$

where the coefficients A_{11} , A_{12} , A_{22} and A_{66} are the elastic constants of the sidewall material, while ϵ_{11} , ϵ_{12} , ϵ_{22} and γ_{12} are the (dynamical) strains. In terms of the ‘engineering constants’ introduced in Section 4,

$$A_{11} = \frac{E_1 h}{1 - \nu_{12}\nu_{21}}, \quad A_{22} = \frac{E_2 h}{1 - \nu_{12}\nu_{21}}; \quad (41)$$

$$A_{12} = \nu_{21}A_{11} = \nu_{12}A_{22}; \quad (42)$$

$$A_{66} = G_{12}h. \quad (43)$$

The strains are expressible in terms of the displacements and the geometric parameters, *viz.*

$$\epsilon_{11} = \frac{1}{\alpha_1} \frac{\partial u_1}{\partial \theta} + \kappa_g u_2 + \kappa_1 u_3; \quad (44)$$

$$\epsilon_{22} = \frac{1}{\alpha_2} \frac{\partial u_2}{\partial \phi} + \kappa_2 u_3; \quad (45)$$

$$\gamma_{12} = \frac{1}{\alpha_2} \frac{\partial u_1}{\partial \phi} - \kappa_g u_1 + \frac{1}{\alpha_1} \frac{\partial u_2}{\partial \theta}. \quad (46)$$

The pre-stress contribution has terms that are both linear and quadratic in the components of \mathbf{u} . The former contribute to the steady equilibrium equations, and are irrelevant here. The latter are:

$$U_p = \frac{1}{2} \int_{-\phi_r}^{\phi_b} \int_0^{2\pi} N_{22} \left[\left(\frac{1}{\alpha_2} \frac{\partial u_1}{\partial \phi} \right)^2 + \left(\frac{1}{\alpha_2} \frac{\partial u_3}{\partial \phi} - \kappa_2 u_2 \right)^2 \right] \alpha_1 \alpha_2 d\theta d\phi. \quad (47)$$

Finally, again discarding linear contributions, the pressurisation potential is

$$U_a = -\frac{p}{2} \int_{-\phi_r}^{\phi_b} \int_0^{2\pi} \left[\frac{1}{\alpha_1} \left(u_3 \frac{\partial u_1}{\partial \theta} - u_1 \frac{\partial u_3}{\partial \theta} \right) + \frac{1}{\alpha_2} \left(u_3 \frac{\partial u_2}{\partial \phi} - u_2 \frac{\partial u_3}{\partial \phi} \right) \right. \\ \left. + \kappa_1 (u_1^2 + u_3^2) + \kappa_2 (u_2^2 + u_3^2) + \kappa_g u_2 u_3 \right] \alpha_1 \alpha_2 d\theta d\phi. \quad (48)$$

5.2. Discretised variational formulation

Hamilton's principle (see, for example, [14, Chapter 2]) states that

$$\int \delta(U - T)dt = \int \delta W dt, \quad (49)$$

where W is the work function associated with the applied forces. Here these are the reactions f_1 , f_2 , f_3 applied by the belt, and we have

$$W = \int_0^{2\pi} [f_1 u_1 + f_2 u_2 + f_3 u_3]_{\phi=\phi_b} \alpha_1 d\theta. \quad (50)$$

The variational nature of Eq. (49) lends itself naturally to numerical approaches that expand \mathbf{u} in terms of basis functions, of which the waveguide Finite-Element Method is an obvious choice. A piecewise linear (in the meridional direction) representation of \mathbf{u} , however, was found to lead to a scheme with poor convergence properties, so a higher-order approach was employed. As this differs from a standard higher-order FE implementation, it is documented here.

The displacement components are written in terms of (the Fourier components of) their values and meridional gradients at the $K + 1$ nodal points of the discretisation. Thus, for example,

$$u_1(\theta, \phi) = \sum_{n=-\infty}^{\infty} \sum_{k=1}^{K+1} e^{in\theta} \left[u_1^{kn} V_k(\phi) + u_{1\phi}^{kn} W_k(\phi) \right], \quad (51)$$

with the basis functions V_k and W_k defined by the requirement that

$$\begin{aligned} V_k(\phi = \phi_l) = \frac{dW_k}{d\phi} \Big|_{\phi=\phi_l} &= 1, & l = k; \\ &= 0, & \text{otherwise;} \end{aligned} \quad (52)$$

and

$$\frac{dV_k}{d\phi} \Big|_{\phi=\phi_l} = W_k(\phi = \phi_l) = 0, \quad \forall l. \quad (53)$$

This form is thus continuous to one order higher than the basic, piecewise-linear, FE expansion. On substituting it into Eq. (49), we obtain the discretised variations set out in Appendix C, and Hamilton's principle becomes

$$\left(\delta \mathbf{d}^{(n)} \right)^H \left[\mathbf{M} \ddot{\mathbf{d}}^{(n)} + 2\Omega \mathbf{C} \dot{\mathbf{d}}^{(n)} + \left(\mathbf{K} - \Omega^2 \mathbf{M}^{(c)} \right) \mathbf{d}^{(n)} \right] = \left(\delta \mathbf{d}^{(n)} \right)^H \mathbf{f}^{(n)}, \quad (54)$$

in which $\mathbf{d}^{(n)}$ is the column vector of nodal displacements and gradients at azimuthal order n (cf. Eq. (51)), and an 'H' superscript indicates the Hermitian transpose. The term in square brackets contains: a standard mass matrix \mathbf{M} and a centrifugal mass matrix $\mathbf{M}^{(c)}$, both real and symmetric; a real, skew-symmetric, Coriolis matrix \mathbf{C} ; and a Hermitian stiffness matrix \mathbf{K} . The (column) vector $\mathbf{f}^{(n)}$ on the right-hand side has non-zero entries at indices $K + 1$, $3(K + 1)$ and $5(K + 1)$ only, these being $R_b f_1^{(n)}$, $R_b f_2^{(n)}$ and $R_b f_3^{(n)}$ respectively.

In all the cases to be considered, the sidewall is fixed at the rim, i.e. $u_1 = u_2 = u_3 = 0$ there, and there are no admissible variations in these quantities. For verification purposes, we will

investigate the natural frequencies and mode shapes when the belt edge is also fixed. The absence of admissible variations in u_1 , u_2 and u_3 there results in the right-hand side of Eq. (54) vanishing, while the arbitrariness of the remaining variations implies that

$$\left[\mathbf{M}\ddot{\mathbf{d}}^{(n)} + 2\Omega\mathbf{C}\dot{\mathbf{d}}^{(n)} + \left(\mathbf{K} - \Omega^2\mathbf{M}^{(c)} \right) \mathbf{d}^{(n)} \right]'' = 0. \quad (55)$$

(Here the double-dash superscript indicates that all matrix rows and columns corresponding to edge displacements — 1, $K + 1$, $2(K + 1) + 1$, $3(K + 1)$, $4(K + 1) + 1$, $5(K + 1)$ — have been excised.) In the absence of rotation, this reduces to the standard generalised eigenvalue problem for the matrices \mathbf{K} and \mathbf{M} , with the (radian) natural frequencies given by the square roots of the eigenvalues. Solutions are presented in Section 6.

For coupling to a belt model, the belt-edge displacement response to harmonic forcing at radian frequency ω is needed. In this case, Eq. (54) leads to

$$\left[-\omega^2\mathbf{M} + 2i\omega\Omega\mathbf{C} + \mathbf{K} - \Omega^2\mathbf{M}^{(c)} \right]' \mathbf{d}^{(n)} = \mathbf{f}^{(n)}, \quad (56)$$

the single-dash superscript indicating deletion of only rim-edge rows and columns in the matrices. Once this equation is solved for $\mathbf{d}^{(n)}$, the belt-edge displacements can straightforwardly be extracted. The results are characterised by the admittances

$$Y_{ij} = u_i^{(K+1)n} / f_j^{(n)}. \quad (57)$$

Note that, since the matrix in Eq. (56) is Hermitian, $Y_{ji} = Y_{ij}^*$.

6. Verification of the dynamical calculation

6.1. Comparison against exact analytical solutions

Under suitable boundary conditions, the mode shapes of pressurised cylindrical shells can be expressed in simple analytical form (cf., for example, Ref. [15]). The toroidal geometry considered here effectively tends to cylindrical for large enough values of the tyre radius, R . The corresponding infinite cylinder has analytical modes for boundary conditions at $\phi = -\phi_r$ and $\phi = \phi_b$ that are fixed in the 1 and 3 directions, and free for meridional (2) displacements. These modes should match those of the large radius torus (with uniform material properties) when their axial wavenumber is equal to one of the discrete torus set n/R_c .

This observation was used to provide an initial check on the sidewall dynamical model. Convergence of resonance frequencies with increasing R_c (with n/R_c held fixed) was found to be straightforwardly achievable without numerical difficulties, and the resulting values were in exact agreement with their analytical counterparts for all parameter sets tested. The corresponding mode shapes were similarly as expected.

6.2. Comparison against FE computations

A modal analysis was performed on the FE model used in the statical calculations (see Section 2). Since this option is restricted to classical, stationary, mode shapes, results were generated for non-rotating cases only. Both the uniform and varying thickness sidewall geometries were analysed, using the 500×50 element mesh. Convergence was assessed for the uniform thickness case resonance frequencies by comparing against results for 250×25 and 125×13 elements. For the azimuthal orders presented here, the worst-case error is 0.12%.

Azimuthal order		0	1	2	3	4	5
First mode	FE	239.27	240.63	244.67	251.25	260.16	271.17
	sidewall model	241.59	243.01	247.23	254.10	263.40	274.87
	% difference	1.0	1.0	1.0	1.1	1.2	1.4
Second mode	FE	394.55	394.45	394.16	393.72	393.19	392.64
	sidewall model	394.96	394.86	394.58	394.16	393.65	393.11
	% difference	0.10	0.10	0.11	0.11	0.12	0.12

Table 5: Comparison of resonance-frequency predictions (in Hz) from FE computation and from the dynamical sidewall model; uniform-thickness case.

The dynamical sidewall model was also run with 50 elements, for consistency with the FE. Its convergence is, however, much more rapid; for this resolution, the resonance values are accurate to better than 0.0025%.

Table 5 compares the calculated resonance frequencies for the first two modes at each of azimuthal orders 0–5. For the first mode the dynamical sidewall model’s predictions are consistently about 1% higher than those of the FE computation. For the second mode, the differences are much smaller; in the region of 0.1%. This is close to (and in the right direction for) the FE discretisation error estimated from the convergence study.

The associated mode shapes, normalised so that

$$\frac{1}{2K} \sum_{k=1}^{K+1} \left(|u_1^{kn}|^2 + |u_2^{kn}|^2 + |u_3^{kn}|^2 \right) = 1, \quad (58)$$

are plotted in Figures 12 and 13. Within the limits of graphical resolution, the overlay between the FE and dynamical sidewall model results is exact. Note that, as one would expect from the form of the stiffness matrix (see Appendix C.2), the displacements in the meridional (or cross-sectional) plane are complex numbers with the same phase, which differs from that of the azimuthal displacements by $\pm\pi/2$. In other words, the azimuthal maxima and minima of these motions are in quadrature. For the special case $n = 0$, they are entirely decoupled; the first mode is purely azimuthal, and the second purely cross-sectional.

This observation suggests that the discrepancies in the first mode resonance frequencies may be partly due to the differences in the material constants A_{11} and G_{12} between the ABAQUS and current formulations (see Section 4). To test this hypothesis, the code was temporarily modified to employ the ABAQUS values, and this reduced the resonance frequency discrepancy to 0.55% across all azimuthal orders. The source of this residual disagreement has not been identified; however, the possibility that it arises from inconsistencies in the calculated pre-stress parameters has been eliminated.

Similar behaviour is observed in the resonance frequency comparison for the varying thickness case (Table 6). The associated mode shapes are very similar to those for uniform thickness and the model agreement is again perfect at the graphical level. Note that the single-lobed nature of the azimuthal modes makes their resonance frequencies notably more sensitive to thickness variation than those of the cross-sectional modes.

Overall, then, the agreement between the dynamical sidewall model and FE calculations is excellent. However, given that the comparison is between nominally identical physical representations, it might be argued that the residual discrepancies in azimuthal mode resonance frequencies

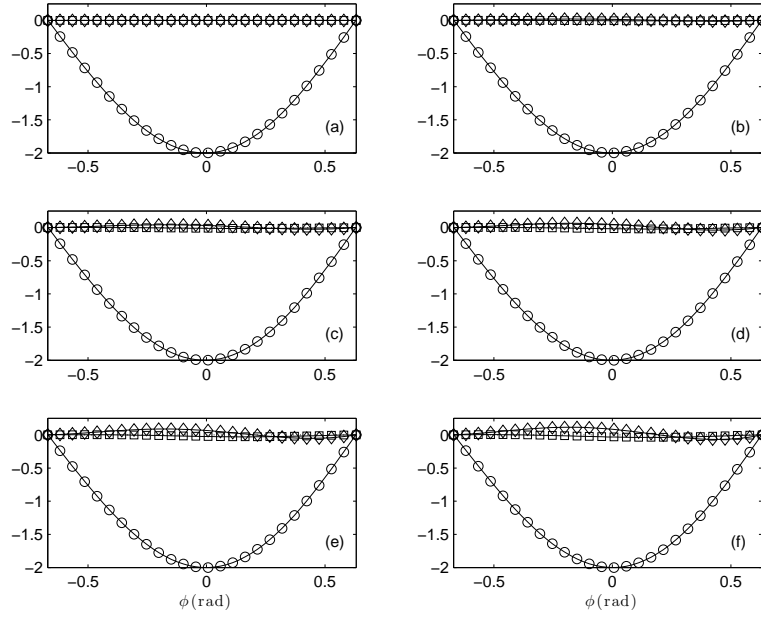


Figure 12: Displacement amplitudes in the uniform-sidewall first mode at azimuthal orders 0 (a) to 5 (f). Lines show results from current model, symbols those from FE (subsamped for clarity). \circ : $\text{Im}(u_1^{kn})$; \square : $\text{Re}(u_2^{kn})$; \diamond : $\text{Re}(u_3^{kn})$. Note that $\text{Re}(u_1^{kn}) = \text{Im}(u_2^{kn}) = \text{Im}(u_3^{kn}) = 0$.

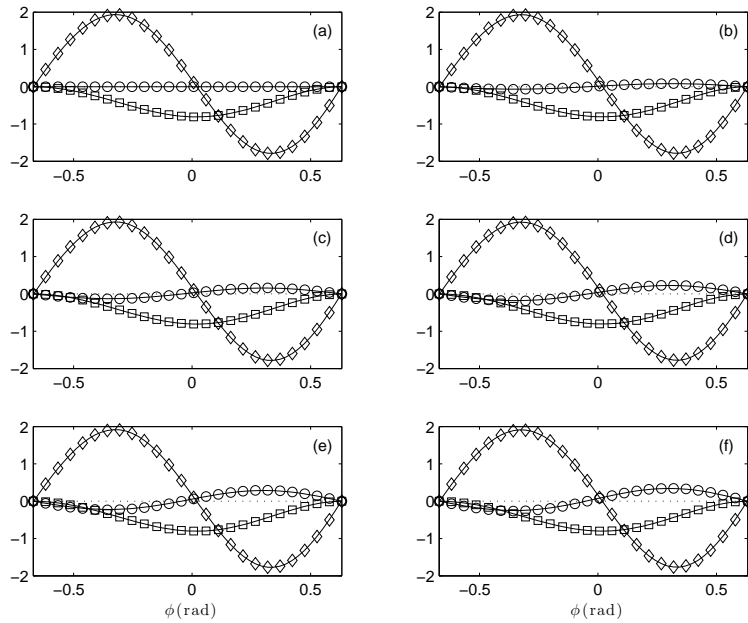


Figure 13: Displacement amplitudes in the uniform-sidewall second mode at azimuthal orders 0 (a) to 5 (f). Legend as Fig. 12.

Azimuthal order		0	1	2	3	4	5
First mode	FE	255.49	256.77	260.56	266.76	275.18	285.61
	sidewall model	258.05	259.39	263.38	269.87	278.70	289.63
	% difference	1.0	1.0	1.1	1.2	1.3	1.4
Second mode	FE	397.06	396.97	396.70	396.31	395.83	395.33
	sidewall model	397.53	397.44	397.18	396.80	396.34	395.85
	% difference	0.12	0.12	0.12	0.12	0.13	0.13

Table 6: Comparison of resonance-frequency predictions (in Hz) from FE computation and from the dynamical sidewall model; varying thickness case.

are unexpectedly high at around 0.5%. While this point carries some weight, the impeccable agreement for the corresponding mode shapes suggests that it is not significant. The current model can thus now be used to investigate the boundary conditions presented by the sidewall to the tyre belt, as characterised by the admittances.

6.3. Computational cost

As for the pre-stress calculation, it is instructive to compare the computational demands of the current model and the commercial FE package. This is less straightforward for the modal analysis, because the FE calculation cannot practically return the full mode set, and does not allow the azimuthal order to be specified. Thus, to find the second modes shown in this section, it was necessary to skip a large number of higher-order first modes, many of which are spurious due to under-resolution. In contrast, the current model (as implemented) computes the full eigenvalue/vector decomposition for the matrices \mathbf{K} and \mathbf{M} at the chosen orders. Nonetheless, its efficiency benefits can be gauged to some extent from the following.

To find the modes corresponding to the first line of Table 6, the first 13 resonance frequencies are requested from the FE calculation. This adds a further 19.7s to the execution time specified in Section 4.4. The full eigenvalue/vector decomposition for the same azimuthal orders takes 3.4s, of which 1.2s is required to assemble the matrices. The waveguide discretisation thus delivers a substantial advantage, even in this unequal comparison.

7. Results

In this section, the full, two-dimensional, model is used to assess the importance, or otherwise, of various features of the sidewall representation. The first is the fundamental change from the one-dimensional model, which neglects both the toroidal nature of the geometry and the influence of azimuthal dependence. It is considered, for the simplest case of uniform sidewall thickness, in Section 7.1. Next, the impact of varying sidewall thickness is investigated, in Section 7.2. Finally, rotation effects are characterised in Section 7.3. The implications of the results for tyre vibration modelling are then discussed.

7.1. Azimuthal dependence

Fig. 14 shows the admittances calculated by the one- and two-dimensional models for the standard test case, over the frequency range 0–400Hz. Note that, for simplicity, no damping is assumed; resonance peak values are limited only by the (1Hz) resolution of the evaluations.

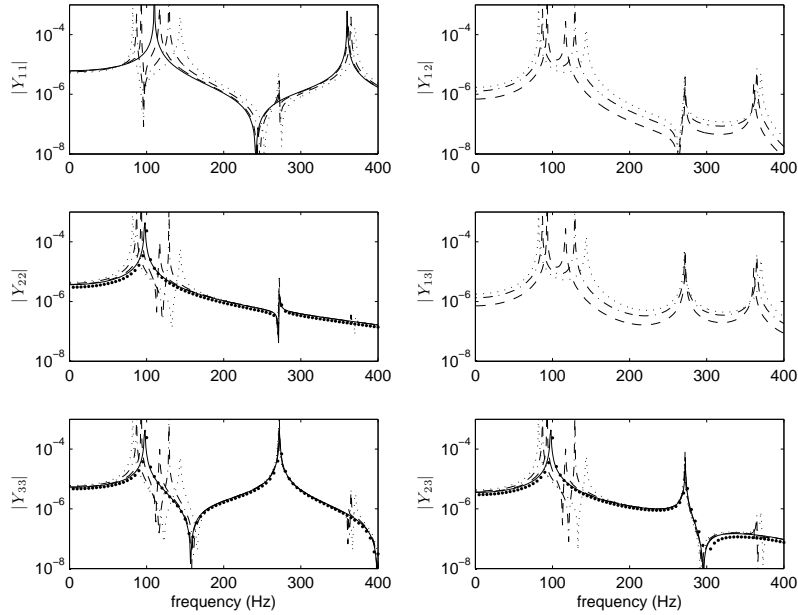


Figure 14: Admittance components for the uniform sidewall. —: $n = 0$; - -: $n = 1$; - · - : $n = 2$; · · · : $n = 3$; ●: one-dimensional model (Y_{22} , Y_{33} and Y_{23} only).

The term ‘azimuthal dependence’ is used here not just for the influence of azimuthal order, n , but also for the change in geometry from the (implicit) infinite cylinder of the one-dimensional representation (including the associated alteration in the pre-stressed base state). The significance of the latter can be isolated by comparing the axisymmetric, $n = 0$, component against the one-dimensional results. This comparison is available for the cross-sectional plane admittances, i.e. Y_{22} , Y_{33} and Y_{23} . For each, there is close agreement, implying that geometrical and base-state details are relatively unimportant.

The two-dimensional model also provides the azimuthal impedance, Y_{11} , for $n = 0$. This parameter exhibits its first resonance peak at a frequency only slightly above the 98Hz value observed for the cross-sectional motions.

The influence of azimuthal order can be assessed from the results for $n = 1 - 3$. Unsurprisingly, these show significant, and increasing, shifts in the first azimuthal resonance frequency. However, they also exhibit departures from the axisymmetric data for the cross-sectional motions. This is unexpected, given the dominance of meridional stiffness and pre-tension. The direction of the shift is also unusual; it corresponds to *decreasing* modal stiffness with increasing azimuthal order.

The other obvious upshot of a non-zero azimuthal order is the introduction of coupling between azimuthal and cross-sectional motions. The plots for Y_{12} and Y_{13} suggest that its levels are non-negligible, and this is confirmed by the appearance of additional resonance peaks in the diagonal impedance components.

Further insight into the azimuthal dependence can be obtained by considering a case where the sidewall is stiffened in this direction via an increase in the rubber Young’s modulus. This is not a purely artificial parameter variation; the elastic properties of rubber are frequency dependent, and the ‘dynamic modulus’ can be two or more times the static value at frequencies of practical interest [6, Chapter 1]. Thus, for this calculation, the (statical) base state is unaltered from the

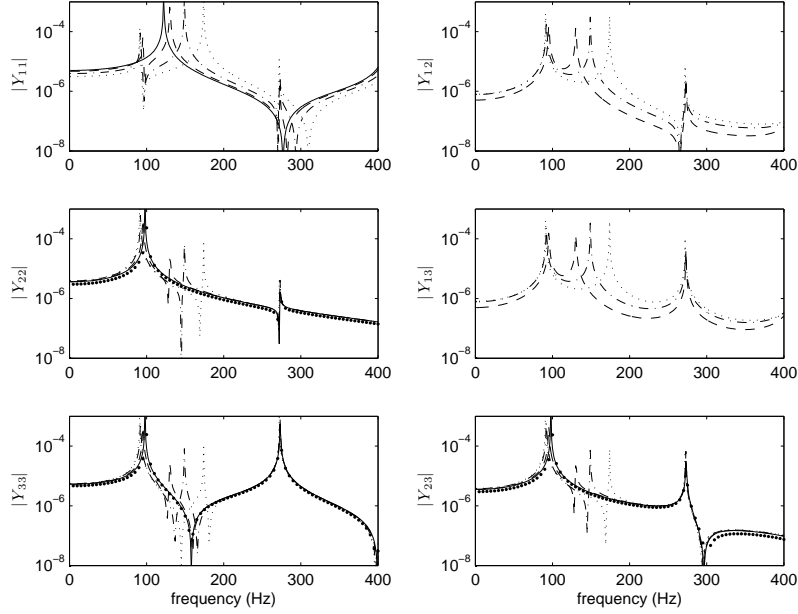


Figure 15: Admittance components for the uniform sidewall with dynamically stiffened rubber modulus. —: $n = 0$; - -: $n = 1$; - · -: $n = 2$; · · · : $n = 3$; ●: one-dimensional model (Y_{22} , Y_{33} and Y_{23} only).

standard case, but $E_r = 5\text{MPa}$ is then used to calculate the material properties. The results are shown in Fig. 15.

It is immediately obvious that the azimuthal stiffening has resulted in an upwards shift in resonance frequencies for the (predominantly) azimuthal modes, as one would expect. Equally intuitively plausible is that the effect on the cross-sectional resonances is much less marked. There is, however, a noteworthy feature: the azimuthal dependence of these modes has been significantly reduced. This suggests that the anomalous dependence noted in the standard case can be ascribed to interaction with the azimuthal modes, and that the one-dimensional calculation will provide good resonance-peak predictions for all orders when the azimuthal resonances are well separated from the cross-sectional. Interaction at the azimuthal resonance frequencies remains evident, though.

7.2. Thickness variation

In practice, sidewalls vary significantly in thickness, with thicker regions at the rim and belt edges. To assess the importance of accurate thickness representation, the diagonal admittance components for the standard case are compared with their counterparts for the varying thickness case. Similar behaviour is seen across all azimuthal orders; here those for $n = 2$ are shown (Fig. 16). The frequency range has been extended to 1kHz, as thickness variation is expected to be more important for higher modes.

This expectation is confirmed by Fig. 16; below about 500Hz, the admittance components for the varying thickness case only differ when their levels are very small, whereas significant differences in resonance peaks are apparent by 1kHz.

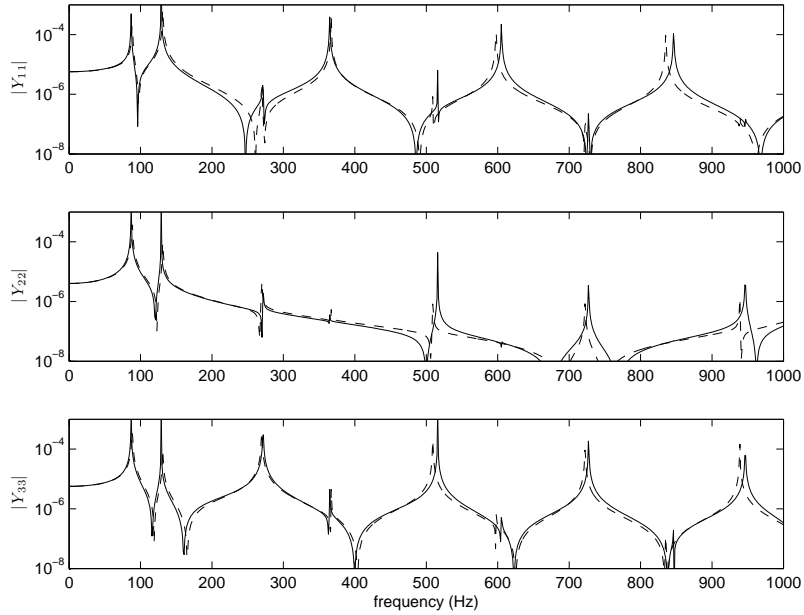


Figure 16: Diagonal admittance components for the uniform (—) and varying thickness (---) sidewalls. Azimuthal order $n = 2$.

7.3. Rotation

As our coordinate system is fixed in the tyre, the effects of rotation are due solely to the additional inertial forces — centrifugal and Coriolis — that are involved. Note, however, that centrifugal forces enter twice: indirectly via their influence on the pre-stress state, and directly via the matrix $\mathbf{M}^{(c)}$. The latter has a softening effect, while the increased tensions associated with rotation should stiffen the sidewall.

There is no reason to anticipate rotation influence to vary significantly with azimuthal order, and inspection of the calculation output confirms that it does not. For this reason, attention will be restricted to the only order where the qualitative form of the admittance is altered: $n = 0$, for which rotation introduces coupling between azimuthal and cross-sectional motions. Fig. 17 shows the $n = 0$ admittances for the standard case and two rotational speeds. The first, $\Omega = 104\text{rads}^{-1}$, corresponds to a vehicle speed of 130km/hour (the ‘with rotation’ case defined in Section 2.4). The second is double this, in order to emphasise differences from the standard case. The frequency range has reverted to the original 0-400Hz, because the proportion of the inertial forces associated with rotation becomes progressively smaller with increasing frequency.

The immediate conclusion from Fig. 17 is that the overall influence of rotation is remarkably small; even at the extreme speed, very little shift in the resonance peaks is evident. At first sight, this is surprising, given that the proportional change in tyre-belt natural frequencies due to rotation is $O(\Omega/\omega)$ [16, 17]. This finding rests, however, on the near-inextensibility of the belt. In contrast, the sidewall is extremely compliant in the azimuthal direction, and this clearly reduces the rotational influence. An analytical estimate of its extent is possible, based on a perturbation approach, and the analysis is straightforward for the $n = 0$ case (Appendix D). It shows that the proportional shift in resonance frequency is in fact $O(\Omega^2/\omega^2)$ here. Further investigation also confirms the expected offsetting influence of centrifugal stiffening of the base state. The upshot is

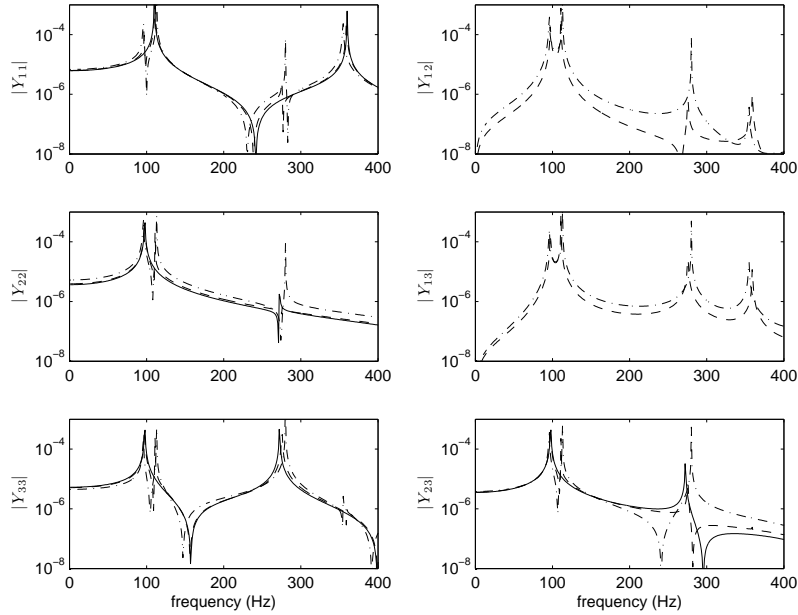


Figure 17: Influence of rotation on $n = 0$ admittance components for the uniform sidewall. —: 0 km/hour; - -: 130 km/hour; -·-: 260km/hour

the rather minimal effect of speed that is evident in Fig. 17, at least for the diagonal admittance components.

The introduction by rotation of non-zero components coupling the axisymmetric azimuthal and cross-sectional motions has already been noted. For the mode shapes, the perturbation analysis suggests a relative change of $O(\Omega/\omega)$, i.e. significantly greater than that in the resonance frequencies. This is clearly borne out by the results of Fig. 17. The plot for Y_{23} , however, suggests that the modification to pre-existing coupling (present on all components for $n \neq 0$) is in general relatively small.

7.4. Discussion

The results presented here show that, while the one-dimensional model is accurate over most of the frequency range in most cases, the full two-dimensional representation is necessary to provide a complete and reliable characterisation of the sidewall admittance. Even when the first azimuthal and cross-sectional resonances are well separated, and the cross-sectional resonance is quite well predicted by the one-dimensional model, the full representation shows significant departures at the azimuthal resonance frequency. These will be smoothed out to some extent in practice by damping, but may not be wholly eliminated. Moreover, without the full representation it is impossible to say that the azimuthal resonance is not close to the cross-sectional; if it is, the one-dimensional model loses accuracy even for the cross-sectional resonances. Despite these comments, however, the one-dimensional representation may well be acceptable, depending on the application.

If one accepts the need for the full model, it has several benefits. The first is the provision of the azimuthal admittance, which must otherwise be treated in an *ad hoc* manner [2]. The second is that meridional non-uniformity is straightforwardly representable. While this aspect does not appear significant for the material stiffness and the tension, it is potentially important for the mass

distribution. In particular, for the example considered here, the sidewall thickness needs to be accurately described if frequencies above about 500Hz are of interest.

Finally, rotational effects also contribute non-uniformly in the meridional direction. Given the relatively minor influence that they have been found to exert, the ability of the full model to account for them may seem irrelevant. However, as they are thought to be potentially important for the belt, it may be necessary to include them in the sidewall description in order to guarantee a self-consistent model of the complete tyre.

7.5. Neglected phenomena

The results presented here have neglected damping, and have only considered frequency dependence in material properties via a uniform ‘dynamic modulus’. It should be noted, however, that these restrictions are not imposed by the model formulation; the two features can straightforwardly be included in Eq. (56). (In the case of damping, this would be by assigning a small imaginary part to the elastic constants.)

In contrast, the membrane representation, with its associated neglect of bending stiffness, is inherent to the model. Its validity can, however, be assessed. Consider the uniform, 7.5mm thick, sidewall, and note that the bending stiffness is dominated by material far from the central plane, i.e. rubber. Taking this to have modulus equal to our dynamic value (5MPa), and neglecting any asymmetry in the cord placement, we have a bending stiffness $D = Eh_s^3/12(1 - \nu^2)$ of 0.23Nm. The associated wavenumber (for free waves on an infinite plane) is $k_p = (M\omega^2/D)^{1/4}$. This can be compared with the corresponding (uniform-tension) membrane wavenumber $k_m = (M\omega^2/pR_s)^{1/2}$. For the parameters used in this paper, the frequency at which the two become equal is 2150Hz. This is well above the frequency range of interest, implying that membrane contributions will indeed dominate. We argue that this conclusion should hold in general, discounting ‘run-flat’ tyres, which have much thicker and stiffer sidewalls.

8. Conclusions

This paper has presented a geometrically accurate model for the vibrations of a tyre sidewall. The sidewall has been represented by a fibre-reinforced membrane, with fixed circular edges at the rim and belt junctions, and an initially toroidal geometry. First, the deformation of this geometry under the steady loadings associated with pressurisation and rotation has been investigated. The results have then been used to provide a base state for a linear vibration analysis.

Finite-Element (FE) calculations for the base state show that the pressurised sidewall remains approximately toroidal, but that the stress field differs significantly from the theoretical solution for a pure toroid. This is mainly because of the strong material anisotropy, due to which the azimuthal stress is negligible in comparison to its meridional counterpart. The latter is comparable to the theoretical prediction in overall level, but not in its detailed variation. Steady rotation (at a rate corresponding to 130km/hour) causes further departures from a toroidal geometry, and has a noticeable influence on the variation (but not the overall level) of the meridional tension. The (meridional) thickness distribution is, however, rather unimportant, with almost no differences evident between a representative example and its mean value applied uniformly.

Analytical approximations for the pressurised sidewall displacement and stress fields have been developed on the basis of a perturbation analysis, relative to an ‘equivalent’ toroid with the same length in the meridional plane as the loaded sidewall. The approach also neglects azimuthal tension entirely. The resulting expressions for the meridional tension show excellent agreement with the

FE output, and can therefore be used in its place to provide the base state for sidewall vibration analysis.

The derivation of explicit formulae for the elastic constants implicit in the FE representation of the reinforced membrane has also been addressed. (This information is necessary in order to apply the analytical approximations independently of any supporting FE.) The FE representation has been interrogated via a set of test cases to yield numerical values, which have been compared against predictions from the standard ‘mixture-rule’ and Halpin-Tsai formulae. The agreement is effectively perfect for the Young’s modulus in the reinforcement direction and for the principal Poisson’s ratio, but not for the transverse Young’s modulus and the shear modulus. The latter is better approximated simply by the shear modulus of the rubber matrix itself, while the former is well described by a new formula, derived via a simplified theoretical approach and containing no empirical parameters.

The equations governing the sidewall vibrations have been formulated via Hamilton’s principle, and discretised in ‘waveguide’ form. The results have been verified against FE modal analyses of stationary cases, and excellent agreement has been obtained. The computation has then been used to investigate a number of modelling issues.

First, the admissibility of a decoupled, one-dimensional representation of vibrations in the meridional plane has been assessed. It has been shown that this approach, while typically accurate to a large extent, may be unreliable, because coupling between azimuthal and meridional-plane displacements is significant at some frequencies. It also fails to provide information on azimuthal vibration characteristics. These demerits must be weighed against the advantage of its simplicity when deciding which approach to employ for a given application.

The influences of meridional thickness variation and rotational inertia effects have then been considered, using the full model. Below approximately 500Hz, a sidewall with a typical thickness variation presents essentially the same belt-edge admittances as one of the same mass and uniform thickness. At higher frequencies, differences start to become evident. Rotation, in contrast, appears to be relatively unimportant at vehicle speeds of practical interest.

Turning to numerical efficiency, the current model far out-performs the commercial FE code. A more pertinent comparison, however, is with the waveguide FE approach of Finnveden and Fraggstedt [1]. Although no timings are given in Ref. [1], one would expect it to show similar advantages in the modal analysis, but not in the pre-stress computation. The use of analytical approximations for the latter also simplifies the coding of the vibration analysis method. Finally, recall that the current representation is intended to be coupled to the belt vibration model of Ref. [2]. An indication of the benefits of using this approach, rather than waveguide FE for the full cross-section, can be obtained by comparing the time taken to calculate the sidewall admittances with the time subsequently required for a belt response evaluation. Using 25 sidewall nodes, and 21 ‘measurement’ locations on the belt, the response vectors for a full set of driving force directions (at a single location) are returned in approximately one-third the admittance calculation time.

Acknowledgements

The help of Arul Britto, Allan McRobie, Xianwei Meng and Julian Oscroft in resolving difficulties arising in the FE calculations is gratefully recognised.

Appendix A. Asymptotic analysis of the equilibrium equations

Appendix A.1. Geometric parameters

The metric coefficients of the surface are defined by Eq. (5). The first is straightforwardly evaluated from Eqs. (4) and (2), which give $\partial\mathbf{r}/\partial\theta = \alpha_1\mathbf{e}_\theta$, with

$$\alpha_1 = R_c + (R_s + w_n)\sin\phi + w_\phi\cos\phi. \quad (\text{A.1})$$

Hence, also, $\mathbf{e}_1 = \mathbf{e}_\theta$. For α_2 , we have

$$\frac{\partial\mathbf{r}}{\partial\phi} = \left(R_s + w_n + \frac{dw_\phi}{d\phi}\right)\mathbf{e}_\phi + \left(-w_\phi + \frac{dw_n}{d\phi}\right)\mathbf{e}_n. \quad (\text{A.2})$$

The exact expression that follows from this can be simplified on the basis of our expectation that the departure from circularity represented by w_ϕ and w_n is small, i.e. $w_\phi/R_s, w_n/R_s \ll 1$. Terms involving quadratic products of these parameters and their derivatives will therefore be ignored, subject to later confirmation that they are indeed negligible. Recalling that the circular arc, by definition, has the same length as the deformed shape then gives

$$w_n + \frac{dw_\phi}{d\phi} \simeq 0, \quad (\text{A.3})$$

and

$$\alpha_2 = R_s. \quad (\text{A.4})$$

The associated basis vector is given by

$$\mathbf{e}_2 \simeq \mathbf{e}_\phi - \frac{1}{R_s} \left(w_\phi + \frac{d^2w_\phi}{d\phi^2}\right)\mathbf{e}_n, \quad (\text{A.5})$$

in which the inextensibility condition, Eq. (A.3), has been used to eliminate w_n .

The unit normal to the deformed surface is $\mathbf{e}_1 \times \mathbf{e}_2$, i.e.

$$\mathbf{e}_3 \simeq \frac{1}{R_s} \left(w_\phi + \frac{d^2w_\phi}{d\phi^2}\right)\mathbf{e}_\phi + \mathbf{e}_n, \quad (\text{A.6})$$

correct to linear order. The meridional curvature κ_2 , given by Eq. (6), is evaluated using $\partial/\partial s_2 = \alpha_2^{-1}\partial/\partial\phi$, giving

$$\kappa_2 \simeq \frac{1}{R_s} \left[1 + \frac{1}{R_s} \left(\frac{dw_\phi}{d\phi} + \frac{d^3w_\phi}{d\phi^3}\right)\right]. \quad (\text{A.7})$$

Appendix A.2. Dimensionless form

In preparation for the forthcoming asymptotic analysis, the equilibrium equations must be non-dimensionalised. On defining

$$\alpha = \frac{\alpha_1}{R_s}, \quad N = \frac{N_{22}}{pR_s}, \quad \mu = \frac{M\Omega^2 R_s}{p}, \quad (\text{A.8})$$

Eqs. (7) and (8) become:

$$\frac{d}{d\phi}(\alpha N) = -\mu\alpha^2\mathbf{e}_r \cdot \mathbf{e}_2, \quad (\text{A.9})$$

$$R_s\kappa_2\alpha N = \alpha + \mu\alpha^2\mathbf{e}_r \cdot \mathbf{e}_3. \quad (\text{A.10})$$

Appendix A.3. Analysis

A mathematically rigorous approximate solution to Eqs. (A.9) and (A.10) can be obtained on the basis that the mean sidewall angle,

$$\phi_s = \frac{\phi_r + \phi_b}{2}, \quad (\text{A.11})$$

is small, and the ratio R_s/R_c is of order 1. The dimensionless parameters α and $R_s\kappa_2$ are then evidently also of order 1, and N is expected to be likewise (because $N_{22} = pR_s$ would apply for the stationary tyre with $\phi_s \rightarrow 0$). The centrifugal force parameter μ varies with rotation speed, and is taken to be order 1 for generality.

According to Hinch [18], the asymptotic solution is found by writing the unknown quantities as series of $O(1)$ functions associated with each order of ϕ_s , *e.g.*

$$\frac{w_\phi}{R_s} \sim \sum_{m=m_1}^{\infty} w_\phi^{(m)}(q)\phi_s^m, \quad (\text{A.12})$$

in which

$$q = \phi/\phi_s \quad (\text{A.13})$$

is the normalised meridional coordinate. It is thus $O(1)$, as are the derivatives of the $w_\phi^{(m)}$ with respect to it. This means that

$$\frac{1}{R_s} \frac{d^3 w_\phi}{dq^3} = \phi_s^{-3} \frac{d^3}{dq^3} \left(\frac{w_\phi}{R_s} \right) \sim O(\phi_s^{-3}) O\left(\frac{w_\phi}{R_s} \right), \quad (\text{A.14})$$

and hence that the first non-zero function in (A.12) must have $m = m_1 \geq 4$ in order that the correction to κ_2 in Eq. (A.7) is small, as assumed.

To apply the asymptotic approach, we further assume that μ can be expanded as a Taylor series in ϕ :

$$\mu = \mu^{(0)} + \mu^{(1)}\phi + \mu^{(2)}\phi^2 + \dots \sim \mu^{(0)} + O(\phi_s). \quad (\text{A.15})$$

To $O(\phi_s)$, then, Eq. (A.9) is

$$\frac{d}{dq}(\alpha N) \sim -\mu^{(0)} \left(\frac{R_c}{R_s} \right)^2 \phi_s, \quad (\text{A.16})$$

with solution

$$\alpha N \sim C - \mu^{(0)} \left(\frac{R_c}{R_s} \right)^2 q \phi_s, \quad (\text{A.17})$$

where C is a constant. In the light of our earlier observations on α and N , we must have $C \sim O(1)$, so we write

$$C \sim C^{(0)} + C^{(1)}\phi_s + O(\phi_s^2). \quad (\text{A.18})$$

Now assume that $w_\phi/R_s \sim O(\phi_s^4)$, the largest it can be while still leading to a small correction to κ_2 . Equation (A.7) becomes

$$R_s\kappa_2 \sim 1 + \frac{1}{R_s} \frac{d^3 w_\phi^{(4)}}{dq^3} \phi_s + O(\phi_s^2), \quad (\text{A.19})$$

and, at $O(1)$, Eq. (A.10) is

$$C^{(0)} = \frac{R_c}{R_s}. \quad (\text{A.20})$$

Next, at $O(\phi_s)$, it is

$$\left[C^{(1)} - \mu^{(0)} \left(\frac{R_c}{R_s} \right)^2 q \right] + \frac{C^{(0)}}{R_s} \frac{d^3 w_\phi^{(4)}}{dq^3} = \left[1 + \mu^{(0)} \left(\frac{R_c}{R_s} \right)^2 \right] q, \quad (\text{A.21})$$

to be solved subject to the boundary conditions

$$w_\phi^{(4)} = w_n^{(3)} (= -dw_\phi^{(4)}/dq) = 0 \quad \text{at} \quad q = -q_r (= -\phi_r/\phi_s) \quad \text{and} \quad q = q_b (= \phi_b/\phi_s). \quad (\text{A.22})$$

The result is

$$\frac{w_\phi^{(4)}}{R_s} = \frac{1}{24} \frac{R_s}{R_c} \left[1 + 2\mu^{(0)} \left(\frac{R_c}{R_s} \right)^2 \right] (q + q_r)^2 (q - q_b)^2, \quad (\text{A.23})$$

$$C^{(1)} = -\frac{q_r - q_b}{2} \left[1 + 2\mu^{(0)} \left(\frac{R_c}{R_s} \right)^2 \right]. \quad (\text{A.24})$$

The existence of this unique, non-zero solution for $w_\phi^{(4)}$ confirms the initial assumption, $w_\phi/R_s \sim O(\phi_s^4)$. Note that the analysis is selective over expanding α in terms of ϕ_s , only doing so for the occurrences in the right-hand sides of Eqs. (A.9) and (A.10). There is no rigorous justification for this choice; it is made because the leading-order result that αN is constant is *exact* for the non-rotating tyre, suggesting that the approximate solution may be more accurate if this form is retained. Admittedly, α itself is only known approximately; however, from Eq. (A.1), we have

$$\alpha_1 \sim R_c + R_s \sin \phi + R_s O(\phi_s^4), \quad (\text{A.25})$$

which implies that the approximation $\alpha_1 \simeq R_c + R_s \sin \phi$ should comfortably be acceptable.

In principle, the results presented so far are sufficient to define the base, equilibrium, state for the linear vibration model. However, the analysis is clarified if phrased in terms of three additional derived quantities, namely the meridional, azimuthal and geodesic curvatures: κ_2 , κ_1 and κ_g . Of these, κ_2 has already been considered; from Eqs. (A.19) and (A.23) it is given explicitly by

$$\kappa_2 \sim \frac{1}{R_s} \left[1 + \left(\frac{R_s}{R_c} + 2\mu^{(0)} \frac{R_c}{R_s} \right) \left(\phi + \frac{\phi_r - \phi_b}{2} \right) + O(\phi_s^2) \right]. \quad (\text{A.26})$$

The other two quantities are defined by (cf. Ref. [10])

$$\kappa_g \mathbf{e}_2 + \kappa_1 \mathbf{e}_3 = -\frac{\partial^2 \mathbf{r}}{\partial s_1^2}, \quad (\text{A.27})$$

where s_1 is the azimuthal distance along a line of constant ϕ . From this, the exact representations $\kappa_g = \mathbf{e}_2 \cdot \mathbf{e}_r / \alpha_1$ and $\kappa_1 = \mathbf{e}_3 \cdot \mathbf{e}_r / \alpha_1$ can be evaluated asymptotically by substituting Eqs. (A.5) and (A.6) for \mathbf{e}_2 and \mathbf{e}_3 . The results are:

$$\kappa_g \sim \frac{1}{\alpha_1} \left[\cos \phi - \frac{\sin \phi}{12} \left(\frac{R_s}{R_c} + 2\mu^{(0)} \frac{R_c}{R_s} \right) (6\phi^2 + 6\phi(\phi_r - \phi_b) + \phi_r^2 - 4\phi_r\phi_b + \phi_b^2) + O(\phi_s^4) \right] \quad (\text{A.28})$$

$$\kappa_1 \sim \frac{1}{\alpha_1} \left[\sin \phi + \frac{\cos \phi}{12} \left(\frac{R_s}{R_c} + 2\mu^{(0)} \frac{R_c}{R_s} \right) (6\phi^2 + 6\phi(\phi_r - \phi_b) + \phi_r^2 - 4\phi_r\phi_b + \phi_b^2) + O(\phi_s^3) \right] \quad (\text{A.29})$$

As these expressions give, respectively, the first four and three terms in the asymptotic series, they should provide excellent accuracy. This has been confirmed via direct graphical comparison with the FE results; the curves are almost indistinguishable.

The expression for κ_2 , however, contains only the first two orders. It is compared with the FE results (for which κ_2 follows from $\partial^2 \mathbf{r} / \partial s_2^2$ obtained via numerical differentiation) in Fig. A.18. Although the two are in excellent agreement for the non-rotating case, slight discrepancies towards the boundaries are evident when rotation is included. For this reason, an alternative evaluation — via Eq. (A.10), using the asymptotic results for α , N and \mathbf{e}_3 — is also plotted. This approach yields almost perfect overlay with the FE data in all three cases, and is thus used in preference to Eq. (A.26).

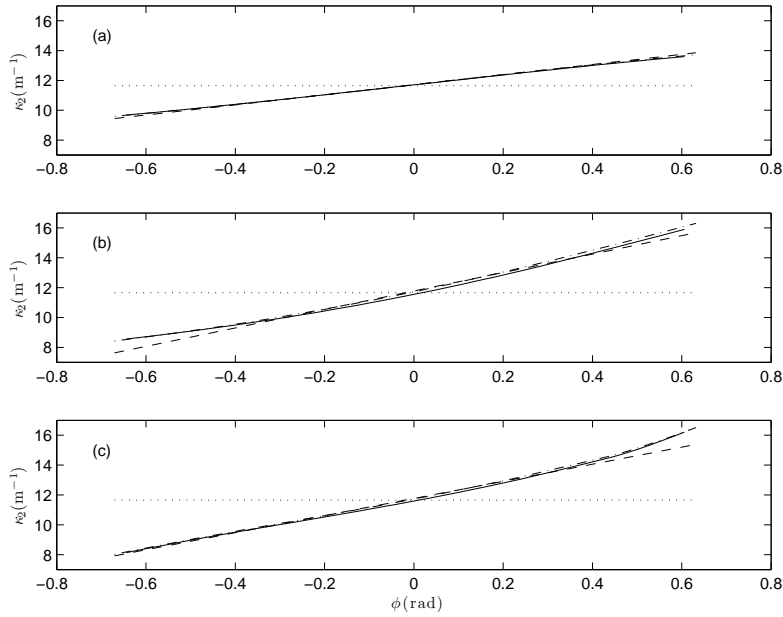


Figure A.18: Meridional curvatures for (a) uniform-thickness, non-rotating; (b) uniform-thickness, rotating; and (c) varying thickness, rotating cases. Comparisons are between FE results (—), analytical approximations (---) and values derived from the analytical approximation to N_{22} (-·-). Dotted lines at $1/R_s$.

Appendix B. Geometrical formulae

The formulation for the equilibrium sidewall shape under pressurisation is set out in Section 3.2, and explicit expressions for the relevant parameters are given in Appendix A. The analysis for the dynamical potential energy components additionally requires the derivatives of the local unit

vectors and metric coefficients with respect to the surface coordinates, θ and ϕ . Exact expressions for these are set out here.

The derivatives of the tangent vectors are directly linked to the surface curvatures. For example, Eq. (A.27) gives

$$\frac{\partial^2 \mathbf{r}}{\partial s_1^2} = -\kappa_g \mathbf{e}_2 - \kappa_1 \mathbf{e}_3, \quad (\text{B.1})$$

while, from the definition of \mathbf{e}_1 , Eq. (5),

$$\frac{\partial^2 \mathbf{r}}{\partial s_1^2} = \frac{\partial \mathbf{e}_1}{\partial s_1} = \frac{1}{\alpha_1} \frac{\partial \mathbf{e}_1}{\partial \theta}. \quad (\text{B.2})$$

Thus

$$\frac{\partial \mathbf{e}_1}{\partial \theta} = -\alpha_1 (\kappa_g \mathbf{e}_2 + \kappa_1 \mathbf{e}_3). \quad (\text{B.3})$$

Similarly, from Eqs. (5) and (6),

$$\frac{\partial \mathbf{e}_2}{\partial \phi} = -\alpha_2 \kappa_2 \mathbf{e}_3. \quad (\text{B.4})$$

The ‘cross’ derivatives, $\partial \mathbf{e}_1 / \partial \phi$ and $\partial \mathbf{e}_2 / \partial \theta$, are also required. The first is identically zero from the choice of coordinates. The second requires the exact expression for the only non-zero derivative of the metric coefficients: $d\alpha_1 / d\phi$. This can be found by considering the geodesic curvature, which, from Eq. (A.27) is given by

$$\kappa_g = -\frac{1}{\alpha_1^2} \mathbf{e}_2 \cdot \frac{\partial^2 \mathbf{r}}{\partial \theta^2} = -\frac{1}{\alpha_1^2 \alpha_2} \frac{\partial \mathbf{r}}{\partial \phi} \cdot \frac{\partial^2 \mathbf{r}}{\partial \theta^2}. \quad (\text{B.5})$$

Now

$$\frac{\partial \mathbf{r}}{\partial \phi} \cdot \frac{\partial \mathbf{r}}{\partial \theta} = 0 \quad (\text{B.6})$$

from the choice of surface coordinates. Differentiating this identity with respect to θ leads to

$$\frac{\partial \mathbf{r}}{\partial \phi} \cdot \frac{\partial^2 \mathbf{r}}{\partial \theta^2} = -\frac{\partial^2 \mathbf{r}}{\partial \phi \partial \theta} \cdot \frac{\partial \mathbf{r}}{\partial \theta} = -\alpha_1 \frac{d\alpha_1}{d\phi}, \quad (\text{B.7})$$

and hence

$$\frac{d\alpha_1}{d\phi} = \alpha_1 \alpha_2 \kappa_g. \quad (\text{B.8})$$

Differentiating Eq. (5) now yields

$$\frac{\partial \mathbf{e}_2}{\partial \theta} = \frac{1}{\alpha_2} \frac{d\alpha_1}{d\phi} \mathbf{e}_1 = \alpha_1 \kappa_g \mathbf{e}_1. \quad (\text{B.9})$$

Appendix C. Derivation of the mass, Coriolis and stiffness matrices

Appendix C.1. The mass and Coriolis matrices

The mass and Coriolis matrices arise from the variation of the kinetic energy expression, Eq. (38). In this term, the perturbation velocity $\partial \mathbf{u} / \partial t$ can be evaluated explicitly with the aid of the observation that $\partial / \partial t = \Omega \partial / \partial \theta$ for the basis vectors. On taking the variation, and integrating by parts where necessary, we have

$$-\int \delta T dt = \int (-\delta T_a) dt + \int (-\delta T_b) dt - \int \delta T_c dt, \quad (\text{C.1})$$

in which

$$-\delta T_a = \int_{-\phi_r}^{\phi_b} \int_0^{2\pi} M \left[\frac{\partial^2 u_1}{\partial t^2} \delta u_1 + \frac{\partial^2 u_2}{\partial t^2} \delta u_2 + \frac{\partial^2 u_3}{\partial t^2} \delta u_3 \right] \alpha_1 \alpha_2 d\theta d\phi, \quad (\text{C.2})$$

$$-\delta T_b = 2\Omega \int_{-\phi_r}^{\phi_b} \int_0^{2\pi} \left[\alpha_1 \left(\kappa_g \frac{\partial u_2}{\partial t} + \kappa_1 \frac{\partial u_3}{\partial t} \right) \delta u_1 - \alpha_1 \kappa_g \frac{\partial u_1}{\partial t} \delta u_2 - \alpha_1 \kappa_1 \frac{\partial u_1}{\partial t} \delta u_3 \right] \alpha_1 \alpha_2 d\theta d\phi, \quad (\text{C.3})$$

$$\delta T_c = \Omega^2 \int_{-\phi_r}^{\phi_b} \int_0^{2\pi} M \left[u_1 \delta u_1 + \alpha_1^2 \kappa_g (\kappa_g u_2 + \kappa_1 u_3) \delta u_2 + \alpha_1^2 \kappa_1 (\kappa_g u_2 + \kappa_1 u_3) \delta u_3 \right] \alpha_1 \alpha_2 d\theta d\phi. \quad (\text{C.4})$$

Note that constant terms multiplying the variations δu_2 and δu_3 have been discarded, since they lead to the steady equations for the mean stress state considered previously.

The displacements and their variations are now discretised in terms of the basis functions introduced in Eq. (51). Specifically, u_1 is written as

$$u_1(\theta, \phi) = \sum_{n=-\infty}^{\infty} \sum_{l=1}^{K+1} e^{in\theta} \left[u_1^{ln} V_l(\phi) + u_{1\phi}^{ln} W_l(\phi) \right], \quad (\text{C.5})$$

and u_2, u_3 similarly. The variations are written in the form

$$\delta u_1(\theta, \phi) = \sum_{m=-\infty}^{\infty} \sum_{k=1}^{K+1} e^{-im\theta} \left[(\delta u_1^{km})^* V_k(\phi) + (\delta u_{1\phi}^{km})^* W_k(\phi) \right], \quad (\text{C.6})$$

where, for convenience in the subsequent analysis, the real nature of δu_1 has been exploited to conjugate the complex quantities on the right-hand side. When these expressions are substituted into Eqs. (C.2)–(C.4), integrals arise of the form

$$\int_{-\phi_r}^{\phi_b} f(\phi) G_k(\phi) H_l(\phi) d\phi, \quad (\text{C.7})$$

in which G_k and H_l can be, respectively, V_k or W_k and V_l or W_l . Such an integral will be represented by the notation $\langle f \rangle_{kl}^{GH}$. Then, for example, Eq. (C.2) can be written as

$$\begin{aligned}
-\frac{\delta T_a}{2\pi} = & \sum_{n=-\infty}^{\infty} \sum_{k=1}^{K+1} \sum_{l=1}^{K+1} \left\{ \left[\left(\delta u_1^{kn} \right)^* \ddot{u}_1^{ln} + \left(\delta u_2^{kn} \right)^* \ddot{u}_2^{ln} + \left(\delta u_3^{kn} \right)^* \ddot{u}_3^{ln} \right] \langle M \alpha_1 \alpha_2 \rangle_{kl}^{VV} \right. \\
& + \left[\left(\delta u_1^{kn} \right)^* \ddot{u}_{1\phi}^{ln} + \left(\delta u_2^{kn} \right)^* \ddot{u}_{2\phi}^{ln} + \left(\delta u_3^{kn} \right)^* \ddot{u}_{3\phi}^{ln} \right] \langle M \alpha_1 \alpha_2 \rangle_{kl}^{VW} \\
& + \left[\left(\delta u_{1\phi}^{kn} \right)^* \ddot{u}_1^{ln} + \left(\delta u_{2\phi}^{kn} \right)^* \ddot{u}_2^{ln} + \left(\delta u_{3\phi}^{kn} \right)^* \ddot{u}_3^{ln} \right] \langle M \alpha_1 \alpha_2 \rangle_{kl}^{WV} \\
& \left. + \left[\left(\delta u_{1\phi}^{kn} \right)^* \ddot{u}_{1\phi}^{ln} + \left(\delta u_{2\phi}^{kn} \right)^* \ddot{u}_{2\phi}^{ln} + \left(\delta u_{3\phi}^{kn} \right)^* \ddot{u}_{3\phi}^{ln} \right] \langle M \alpha_1 \alpha_2 \rangle_{kl}^{WW} \right\}. \quad (\text{C.8})
\end{aligned}$$

This expression can be made much less cumbersome by writing it in matrix/vector form. Let $\mathbf{d}^{(n)}$ be the column vector containing all the displacement and gradient values for azimuthal order n , i.e.

$$\mathbf{d}^{(n)} = \left[u_1^{1n} \cdots u_1^{(K+1)n} u_{1\phi}^{1n} \cdots u_{1\phi}^{(K+1)n} u_2^{1n} \cdots u_2^{(K+1)n} u_{2\phi}^{1n} \cdots u_{2\phi}^{(K+1)n} u_3^{1n} \cdots u_3^{(K+1)n} u_{3\phi}^{1n} \cdots u_{3\phi}^{(K+1)n} \right]^T. \quad (\text{C.9})$$

Also let $\langle M \alpha_1 \alpha_2 \rangle^{GH}$ represent the $(K+1) \times (K+1)$ matrix whose (k, l) th element is $\langle M \alpha_1 \alpha_2 \rangle_{kl}^{GH}$. Then

$$-\frac{\delta T_a}{2\pi} = \sum_{n=-\infty}^{\infty} \left(\delta \mathbf{d}^{(n)} \right)^H \begin{bmatrix} \mathbf{M} & \mathbf{0} & \mathbf{0} \\ \mathbf{0} & \mathbf{M} & \mathbf{0} \\ \mathbf{0} & \mathbf{0} & \mathbf{M} \end{bmatrix} \dot{\mathbf{d}}^{(n)}, \quad (\text{C.10})$$

in which $\mathbf{M} = \langle M \alpha_1 \alpha_2 \rangle^{00}$, with

$$\langle M \alpha_1 \alpha_2 \rangle^{00} = \begin{bmatrix} \langle M \alpha_1 \alpha_2 \rangle^{VV} & \langle M \alpha_1 \alpha_2 \rangle^{VW} \\ \langle M \alpha_1 \alpha_2 \rangle^{WV} & \langle M \alpha_1 \alpha_2 \rangle^{WW} \end{bmatrix}. \quad (\text{C.11})$$

This $2(K+1) \times 2(K+1)$ matrix is symmetrical, as then is the mass matrix of Eq. (C.10). To avoid excess notation, we will also refer to the latter as \mathbf{M} , since the meaning of the symbol will be evident from its context. The relevance of the superscript in the abbreviated notation of Eq. (C.11) will become evident subsequently.

When the same approach is applied to the other two components of the kinetic energy variation, Eqs. (C.3) and (C.4), we obtain

$$-\frac{\delta T_b}{2\pi} = 2\Omega \sum_{n=-\infty}^{\infty} \left(\delta \mathbf{d}^{(n)} \right)^H \begin{bmatrix} \mathbf{0} & \mathbf{C}_{12} & \mathbf{C}_{13} \\ -\mathbf{C}_{12} & \mathbf{0} & \mathbf{0} \\ -\mathbf{C}_{13} & \mathbf{0} & \mathbf{0} \end{bmatrix} \dot{\mathbf{d}}^{(n)}, \quad (\text{C.12})$$

with

$$\mathbf{C}_{12} = \langle M \alpha_1^2 \alpha_2 \kappa_g \rangle^{00}, \quad \mathbf{C}_{13} = \langle M \alpha_1^2 \alpha_2 \kappa_1 \rangle^{00}, \quad (\text{C.13})$$

and

$$\frac{\delta T_c}{2\pi} = \Omega^2 \sum_{n=-\infty}^{\infty} \left(\delta \mathbf{d}^{(n)} \right)^H \begin{bmatrix} \mathbf{M} & \mathbf{0} & \mathbf{0} \\ \mathbf{0} & \mathbf{M}_{22}^{(c)} & \mathbf{M}_{23}^{(c)} \\ \mathbf{0} & \mathbf{M}_{23}^{(c)} & \mathbf{M}_{33}^{(c)} \end{bmatrix} \mathbf{d}^{(n)}, \quad (\text{C.14})$$

with

$$\mathbf{M}_{22}^{(c)} = \langle M\alpha_1^3\alpha_2\kappa_g^2 \rangle^{00}, \quad \mathbf{M}_{23}^{(c)} = \langle M\alpha_1^3\alpha_2\kappa_1\kappa_g \rangle^{00}, \quad \mathbf{M}_{33}^{(c)} = \langle M\alpha_1^3\alpha_2\kappa_1^2 \rangle^{00}. \quad (\text{C.15})$$

The matrix in Eq. (C.12) represents Coriolis terms, and will be denoted \mathbf{C} , while that in Eq. (C.14) arises from centrifugal effects, and will be referred to as $\mathbf{M}^{(c)}$. The components of the former, \mathbf{C}_{12} and \mathbf{C}_{13} , are symmetric, so \mathbf{C} is skew-symmetric. In contrast, $\mathbf{M}_{22}^{(c)}$, $\mathbf{M}_{23}^{(c)}$ and $\mathbf{M}_{33}^{(c)}$ are symmetric, as therefore is $\mathbf{M}^{(c)}$.

Appendix C.2. The stiffness matrix

The stiffness matrix arises from the substitution of the discretised forms of the displacements and their variations into the expression for the variation of the potential energy, giving

$$\frac{\delta U}{2\pi} = \sum_{n=-\infty}^{\infty} \left(\delta \mathbf{d}^{(n)} \right)^H \begin{bmatrix} \mathbf{K}_{11} & \mathbf{K}_{12} & \mathbf{K}_{13} \\ \mathbf{K}_{12}^H & \mathbf{K}_{22} & \mathbf{K}_{23} \\ \mathbf{K}_{13}^H & \mathbf{K}_{23}^H & \mathbf{K}_{33} \end{bmatrix} \mathbf{d}^{(n)}. \quad (\text{C.16})$$

The presence of meridional derivatives in the potential-energy formulae means that the matrix components contain integrals involving not only the basis functions themselves, but also their derivatives with respect to ϕ . This necessitates an extension of the nomenclature introduced in Appendix C.1.

The original notation $\langle f \rangle_{kl}^{GH}$ is extended via dashes in the superscript to indicate differentiated basis functions; e.g.

$$\langle f \rangle_{kl}^{V'W} = \int_{-\phi_r}^{\phi_b} f(\phi) \frac{dV_k}{d\phi} W_l(\phi) d\phi \quad (\text{C.17})$$

and, as previously, the subscript is dropped to indicate the corresponding matrix. The superscript in the block matrix nomenclature that was introduced in Eq. (C.11) is now used to indicate which of the basis functions is differentiated. Thus, continuing the above example,

$$\langle f \rangle^{10} = \begin{bmatrix} \langle f \rangle^{V'V} & \langle f \rangle^{V'W} \\ \langle f \rangle^{W'V} & \langle f \rangle^{W'W} \end{bmatrix}. \quad (\text{C.18})$$

In terms of this notation, the six matrix components of the stiffness matrix are given by

$$\mathbf{K}_{11} = \left\langle \alpha_1\alpha_2 \left(\frac{n^2}{\alpha_1^2} A_{11} + \kappa_g^2 A_{66} - \kappa_1 p \right) \right\rangle^{00} - \langle \alpha_1\kappa_g A_{66} \rangle^{01} - \langle \alpha_1\kappa_g A_{66} \rangle^{10} + \left\langle \frac{\alpha_1}{\alpha_2} (A_{66} + N_{22}) \right\rangle^{11}, \quad (\text{C.19})$$

$$\mathbf{K}_{22} = \left\langle \alpha_1\alpha_2 \left(\kappa_g^2 A_{11} + \frac{n^2}{\alpha_1^2} A_{66} + \kappa_2^2 N_{22} - \kappa_2 p \right) \right\rangle^{00} + \langle \alpha_1\kappa_g A_{12} \rangle^{01} + \langle \alpha_1\kappa_g A_{12} \rangle^{10} + \left\langle \frac{\alpha_1}{\alpha_2} A_{22} \right\rangle^{11}, \quad (\text{C.20})$$

$$\mathbf{K}_{33} = \langle \alpha_1\alpha_2 [\kappa_1^2 A_{11} + 2\kappa_1\kappa_2 A_{12} + \kappa_2^2 A_{22} - (\kappa_1 + \kappa_2)p] \rangle^{00} + \left\langle \frac{\alpha_1}{\alpha_2} N_{22} \right\rangle^{11}, \quad (\text{C.21})$$

$$\mathbf{K}_{12} = -in \langle \alpha_2 \kappa_g (A_{11} + A_{66}) \rangle^{00} - in \langle A_{12} \rangle^{01} + in \langle A_{66} \rangle^{10}, \quad (\text{C.22})$$

$$\mathbf{K}_{13} = -in \langle \alpha_2 (\kappa_1 A_{11} + \kappa_2 A_{12} - p) \rangle^{00}, \quad (\text{C.23})$$

$$\mathbf{K}_{23} = \left\langle \alpha_1 \alpha_2 \kappa_g \left(\kappa_1 A_{11} + \kappa_2 A_{12} - \frac{p}{2} \right) \right\rangle^{00} - \left\langle \alpha_1 \left(\kappa_2 N_{22} - \frac{p}{2} \right) \right\rangle^{01} + \left\langle \alpha_1 \left(\kappa_1 A_{12} + \kappa_2 A_{22} - \frac{p}{2} \right) \right\rangle^{10}. \quad (\text{C.24})$$

The diagonal components, \mathbf{K}_{11} , \mathbf{K}_{22} and \mathbf{K}_{33} , are real and symmetric, so the complex matrix of Eq. (C.16), which will be denoted as \mathbf{K} , is Hermitian symmetric.

Appendix C.3. Matrix assembly

Like the matrices in the standard FE method, those arising here are most straightforwardly assembled element by element. Fig. C.19 shows the k th element, which lies between nodes k and $k + 1$, and its associated basis functions. These are given by

$$V_k = 3(1 - q)^2 - 2(1 - q)^3, \quad V_{k+1} = 3q^2 - 2q^3 \quad (\text{C.25})$$

$$W_k = [(1 - q)^2 - (1 - q)^3] \Delta, \quad W_{k+1} = [-q^2 + q^3] \Delta, \quad (\text{C.26})$$

where Δ is the element ‘length’, $\phi_{k+1} - \phi_k$, and q is its normalised distance variable:

$$q = \frac{\phi - \phi_k}{\Delta}. \quad (\text{C.27})$$

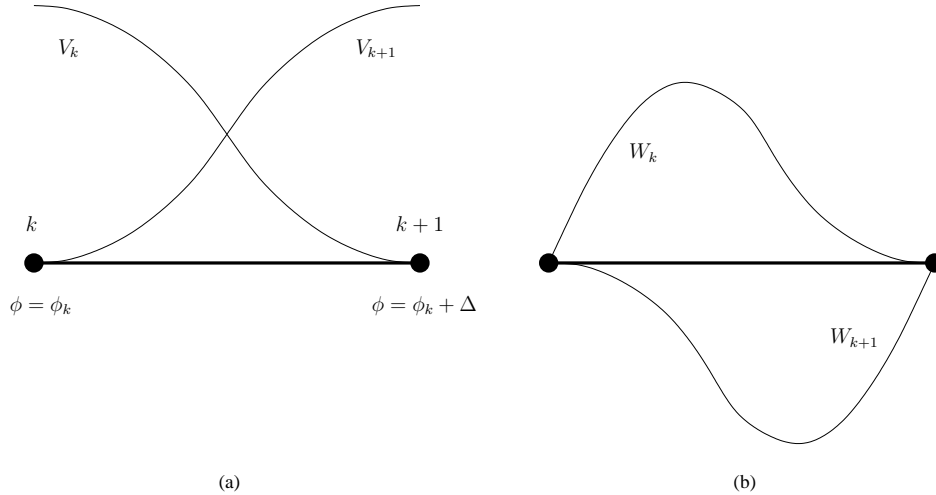


Figure C.19: The basis functions associated with the k th element, which lies between nodes k and $k + 1$. (a) $V_k(\phi)$ and $V_{k+1}(\phi)$; (b) $W_k(\phi)$ and $W_{k+1}(\phi)$.

The k th element contributes to the (k, k) , $(k, k + 1)$, $(k + 1, k)$ and $(k + 1, k + 1)$ entries in each matrix via the four possible shape function products. On the assumption that the ‘argument’

		G,H							
Level of differentiation		V, V		V, W		W, V		W, W	
0, 0	$\frac{\Delta}{70}$	$\begin{bmatrix} 26 & 9 \\ 9 & 26 \end{bmatrix}$	$\frac{\Delta^2}{420}$	$\begin{bmatrix} 22 & -13 \\ 13 & -22 \end{bmatrix}$	$\frac{\Delta^2}{420}$	$\begin{bmatrix} 22 & 13 \\ -13 & -22 \end{bmatrix}$	$\frac{\Delta^3}{420}$	$\begin{bmatrix} 4 & -3 \\ -3 & 4 \end{bmatrix}$	
0, 1	$\frac{1}{2}$	$\begin{bmatrix} -1 & 1 \\ -1 & 1 \end{bmatrix}$	$\frac{\Delta}{10}$	$\begin{bmatrix} 1 & -1 \\ -1 & 1 \end{bmatrix}$	$\frac{\Delta}{10}$	$\begin{bmatrix} -1 & 1 \\ 1 & -1 \end{bmatrix}$	$\frac{\Delta^2}{60}$	$\begin{bmatrix} 0 & -1 \\ 1 & 0 \end{bmatrix}$	
1, 0	$\frac{1}{2}$	$\begin{bmatrix} -1 & -1 \\ 1 & 1 \end{bmatrix}$	$\frac{\Delta}{10}$	$\begin{bmatrix} -1 & 1 \\ 1 & -1 \end{bmatrix}$	$\frac{\Delta}{10}$	$\begin{bmatrix} 1 & -1 \\ -1 & 1 \end{bmatrix}$	$\frac{\Delta^2}{60}$	$\begin{bmatrix} 0 & 1 \\ -1 & 0 \end{bmatrix}$	
1, 1	$\frac{6}{5\Delta}$	$\begin{bmatrix} 1 & -1 \\ -1 & 1 \end{bmatrix}$	$\frac{1}{10}$	$\begin{bmatrix} 1 & 1 \\ -1 & -1 \end{bmatrix}$	$\frac{1}{10}$	$\begin{bmatrix} 1 & -1 \\ 1 & -1 \end{bmatrix}$	$\frac{\Delta}{30}$	$\begin{bmatrix} 4 & -1 \\ -1 & 4 \end{bmatrix}$	

Table C.7: Element matrix contributions. Each 2×2 array represents the additions to (reading along rows first) the (k, k) , $(k, k + 1)$, $(k + 1, k)$ and $(k + 1, k + 1)$ entries in the relevant matrix when the argument f is unity. Columns in the table give the possible basis function combinations and rows their levels of differentiation.

f of our notation (cf. Eq. (C.7)) varies sufficiently slowly to be approximated by its value at the element centre, f_c , the contributions are easily evaluated. They are tabulated (for $f_c = 1$) as 2×2 matrices in Table C.7.

Appendix D. Perturbation analysis for rotating sidewall resonances

The resonances observed in the admittance plots correspond to the unforced solutions of Eqs. (56). For $n = 0$, these can be written in the form

$$\begin{bmatrix} \mathbf{K}_{11} - (\omega^2 + \Omega^2)\mathbf{M} & 2i\omega\Omega\mathbf{C}_{ax} \\ -2i\omega\Omega\mathbf{C}_{ax}^T & \mathbf{K}_x - \omega^2\mathbf{M}_x - \Omega^2\mathbf{M}_x^{(c)} \end{bmatrix} \begin{bmatrix} \psi_a \\ \psi_x \end{bmatrix} = \mathbf{0} \quad (\text{D.1})$$

Here ψ_a and ψ_x represent, respectively, the azimuthal and cross-sectional components of the displacement vector, while

$$\mathbf{C}_{ax} = \begin{bmatrix} \mathbf{C}_{12} & \mathbf{C}_{13} \end{bmatrix}, \quad (\text{D.2})$$

$$\mathbf{K}_x = \begin{bmatrix} \mathbf{K}_{22} & \mathbf{K}_{23} \\ \mathbf{K}_{23}^T & \mathbf{K}_{33} \end{bmatrix}, \quad (\text{D.3})$$

$$\mathbf{M}_x = \begin{bmatrix} \mathbf{M} & 0 \\ 0 & \mathbf{M} \end{bmatrix}, \quad (\text{D.4})$$

and

$$\mathbf{M}_x^{(c)} = \begin{bmatrix} \mathbf{M}_{22}^{(c)} & \mathbf{M}_{23}^{(c)} \\ \mathbf{M}_{23}^{(c)} & \mathbf{M}_{33}^{(c)} \end{bmatrix}. \quad (\text{D.5})$$

In the absence of rotation, the azimuthal and cross-sectional motions decouple, so their respective first resonances, at $\omega = \omega_a$ and $\omega = \omega_x$, correspond to

$$\psi_a = \psi_{a0}, \quad \psi_x = \mathbf{0}, \quad \mathbf{K}_{11}\psi_{a0} = \omega_a^2\mathbf{M}\psi_{a0} \quad (\text{D.6})$$

and

$$\boldsymbol{\psi}_a = \mathbf{0}, \quad \boldsymbol{\psi}_x = \boldsymbol{\psi}_{x0}, \quad \mathbf{K}_x \boldsymbol{\psi}_{x0} = \omega_x^2 \mathbf{M}_x \boldsymbol{\psi}_{x0}. \quad (\text{D.7})$$

The perturbation analysis seeks solutions for $\Omega \neq 0$ which are close to these quantities. The general approach is set out in Chapter 1 of Hinch [18]; here the decoupled nature of the no-rotation equations is used to find simpler expressions.

Consider the solution that corresponds to a perturbation of the azimuthal resonance:

$$\omega = \omega_a(1 + \epsilon), \quad \boldsymbol{\psi}_a = \boldsymbol{\psi}_{a0} + \delta\boldsymbol{\psi}_a, \quad \boldsymbol{\psi}_x = \delta\boldsymbol{\psi}_x. \quad (\text{D.8})$$

On the basis that Ω/ω_a and the perturbation are small, and employing Eq. (D.6), Eq. (D.1) becomes

$$\begin{bmatrix} -(2\epsilon\omega_a^2 + \Omega^2) \mathbf{M} & 2i\omega_a\Omega \mathbf{C}_{ax} \\ -2i\omega_a\Omega \mathbf{C}_{ax}^T & \mathbf{K}_x - \omega_a^2 \mathbf{M}_x \end{bmatrix} \begin{bmatrix} \boldsymbol{\psi}_{a0} \\ \mathbf{0} \end{bmatrix} + \begin{bmatrix} \mathbf{K}_{11} - \omega_a^2 \mathbf{M} & 2i\omega_a\Omega \mathbf{C}_{ax} \\ -2i\omega_a\Omega \mathbf{C}_{ax}^T & \mathbf{K}_x - \omega_a^2 \mathbf{M}_x \end{bmatrix} \begin{bmatrix} \delta\boldsymbol{\psi}_a \\ \delta\boldsymbol{\psi}_x \end{bmatrix} = \begin{bmatrix} \mathbf{0} \\ \mathbf{0} \end{bmatrix} \quad (\text{D.9})$$

The second line now yields the cross-sectional component of the perturbation vector:

$$\delta\boldsymbol{\psi}_x = 2i\omega_a\Omega [\mathbf{K}_x - \omega_a^2 \mathbf{M}_x]^{-1} \mathbf{C}_{ax}^T \boldsymbol{\psi}_{a0}. \quad (\text{D.10})$$

This quantity is thus $O(\Omega/\omega_a)$ relative to $\boldsymbol{\psi}_{a0}$, confirming that it represents a small perturbation when $\Omega/\omega_a \ll 1$.

The shift in the resonance frequency follows from the first line, combined with the observation that $\boldsymbol{\psi}_{a0}^T (\mathbf{K}_{11} - \omega_a^2 \mathbf{M}) \delta\boldsymbol{\psi}_a = \mathbf{0}$ (by virtue of Eq. (D.6)). Thus

$$\epsilon = -\frac{1}{2} \frac{\Omega^2}{\omega_a^2} + i \frac{\Omega}{\omega_a} \frac{\boldsymbol{\psi}_{a0}^T \mathbf{C}_{ax} \delta\boldsymbol{\psi}_x}{\boldsymbol{\psi}_{a0}^T \mathbf{M} \boldsymbol{\psi}_{a0}}, \quad (\text{D.11})$$

which is $O(\Omega^2/\omega_a^2)$. Finally, $\delta\boldsymbol{\psi}_a$ can be obtained from the same equation via the restricted inverse of $(\mathbf{K}_{11} - \omega_a^2 \mathbf{M})$; it is also $O(\Omega^2/\omega_a^2)$ and hence of the same magnitude as the unknown following-order component of $\delta\boldsymbol{\psi}_x$.

Note that Eq. (D.10) implies failure of the small-perturbation assumption if the matrix $[\mathbf{K}_x - \omega_a^2 \mathbf{M}_x]^{-1}$ is close to singular, i.e. if the cross-sectional and azimuthal resonances are very close. As a numerical experiment, the rubber modulus was reduced in order to bring the resonances closer, but it appears impossible to achieve proximity sufficient to cause exaggerated departures from the no-rotation frequencies.

The analysis for the cross-sectional resonance follows an identical approach and yields similar results; the proportional resonance frequency shift is $O(\Omega^2/\omega_a^2)$ and the eigenvector is perturbed at $O(\Omega/\omega_a)$ by a purely azimuthal contribution.

References

- [1] S. Finnveden, M. Fraggstedt, Waveguide finite elements for curved structures. *Journal of Sound and Vibration* 312 (2008) 644–671.
- [2] C. Lecomte, W.R. Graham, M. Dale, A shell model for tyre belt vibrations. *Journal of Sound and Vibration* 329 (2010) 1717–1742.
- [3] K. Larsson, W. Kropp, A high-frequency three-dimensional tyre model based on two coupled elastic layers. *Journal of Sound and Vibration* 253 (2002) 889–908.
- [4] P. Andersson, K. Larsson, Validation of a high frequency three-dimensional tyre model. *Acta Acustica united with Acustica* 91 (2005) 121–131.

- [5] R.J. Pinnington, A wave model of a circular tyre. Part 2: side-wall and force transmission modelling. *Journal of Sound and Vibration* 290 (2006) 133–168.
- [6] S.K. Clark (Ed.), *Mechanics of pneumatic tires (NBS Monograph 122)*. U. S. Government Printing Office, Washington, 1971.
- [7] C. Miller, P. Popper, P.W. Gilmour, W.J. Schaffers, Textile mechanics model of a pneumatic tire. *Tire Science and Technology* 13 (1985) 187–226.
- [8] F. Tabaddor, S.K. Clark, R.N. Dodge, J.M. Perraut, Viscoelastic loss characteristics of cord-rubber composites. *Tire Science and Technology* 14 (1986) 75–101.
- [9] S. Timoshenko, S. Woinowsky-Krieger, *Theory of plates and shells* (2nd Ed). McGraw-Hill, New York, 1959.
- [10] G.A. Korn, T.M. Korn, *Mathematical handbook for scientists and engineers: definitions, theorems and formulas for reference and review* (2nd Ed). McGraw-Hill, New York, 1968.
- [11] W. Soedel, *Vibrations of shells and plates* (3rd Ed). Marcel Dekker, New York, 2004.
- [12] D. Hull, T.W. Clyne, *An introduction to composite materials* (2nd Ed). Cambridge University Press, Cambridge, 1996.
- [13] J.C. Halpin, J.L. Kardos, The Halpin-Tsai equations: a review. *Polymer Engineering and Science* 16 (1976) 344–352.
- [14] H. Goldstein, C.P. Poole, J.L. Safko, *Classical mechanics* (3rd Ed). Pearson Addison-Wesley, Upper Saddle River NJ, 2002.
- [15] Y.-J. Kim, J.S. Bolton, Effects of rotation on the dynamics of a circular cylindrical shell with application to tire vibration. *Journal of Sound and Vibration* 275 (2004) 605–621.
- [16] M. Endo, K. Hatamura, M. Sakata, O. Taniguchi, Flexural vibration of a thin rotating ring. *Journal of Sound and Vibration* 92 (1984) 261–272.
- [17] S.C. Huang, W. Soedel, Effects of Coriolis acceleration on the free and forced in-plane vibrations of rotating rings on elastic foundation. *Journal of Sound and Vibration* 115 (1987) 253–274.
- [18] E.J. Hinch, *Perturbation methods*. Cambridge University Press, Cambridge, 1991.